Available online at www.sciencedirect.com

ScienceDirect

Comput. Methods Appl. Mech. Engrg. 367 (2020) 113124

Computer methods in applied mechanics and engineering

www.elsevier.com/locate/cma

IPACS: Integrated Phase-Field Advanced Crack Propagation Simulator. An adaptive, parallel, physics-based-discretization phase-field framework for fracture propagation in porous media

Mary F. Wheeler[a], Thomas Wick[b,*], Sanghyun Lee[c]

[a] Center for Subsurface Modeling, The Institute for Computational Engineering and Sciences, The University of Texas at Austin, Austin, TX 78712, USA

[b] Leibniz Universität Hannover, Institut für Angewandte Mathematik, AG Wissenschaftliches Rechnen, Welfengarten 1, 30167 Hannover, Germany

[c] Department of Mathematics, Florida State University, 1017 Academic Way, Tallahassee, FL 32306, USA

Abstract

In this work, we review and describe our computational framework for solving multiphysics phase-field fracture problems in porous media. Therein, the following five coupled nonlinear physical models are addressed: displacements (geo-mechanics), a phase-field variable to indicate the fracture position, a pressure equation (to describe flow), a proppant concentration equation, and/or a saturation equation for two-phase fracture flow, and finally a finite element crack width problem. The overall coupled problem is solved with a staggered solution approach, known in subsurface modeling as the fixed-stress iteration. A main focus is on physics-based discretizations. Galerkin finite elements are employed for the displacement-phase-field system and the crack width problem. Enriched Galerkin formulations are used for the pressure equation. Further enrichments using entropy-vanishing viscosity are employed for the proppant and/or saturation equations. A robust and efficient quasi-monolithic semi-smooth Newton solver, local mesh adaptivity, and parallel implementations allow for competitive timings in terms of the computational cost. Our framework can treat two- and three-dimensional realistic field and laboratory examples. The resulting program is an in-house code named IPACS (Integrated Phase-field Advanced Crack Propagation Simulator) and is based on the finite element library deal.II. Representative numerical examples are included in this document.

Keywords: Phase-field fracture; Porous media; Computer implementation; Numerical simulations; Handbook; IPACS

---

1. Introduction

The coupling of flow and geomechanics in fractured porous media is currently a major research area in energy and environmental modeling [1,2]. Specific applications include flow in fractured porous media, the interaction between natural and induced fractures, non-isothermal processes, geothermal energy recovery, and hydraulic fracturing or hydrofracturing commonly known as fracking. In these research fields, the Center for Subsurface Modeling (CSM) at the Oden institute at the University of Texas at Austin, in collaboration with other international institutes, has

---

[*] Corresponding author.
E-mail address: thomas.wick@ifam.uni-hannover.de (T. Wick).

https://doi.org/10.1016/j.cma.2020.113124

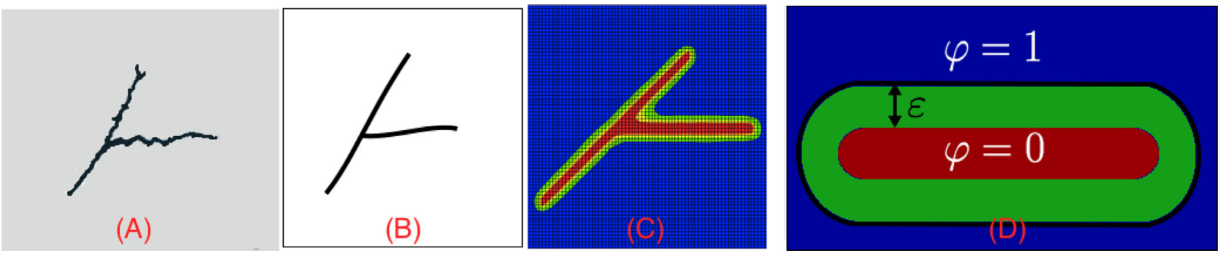

Fig. 1. Representation of the fracture with the phase field function. (For interpretation of the references to color in this figure legend, the reader is referred to the web version of this article.)

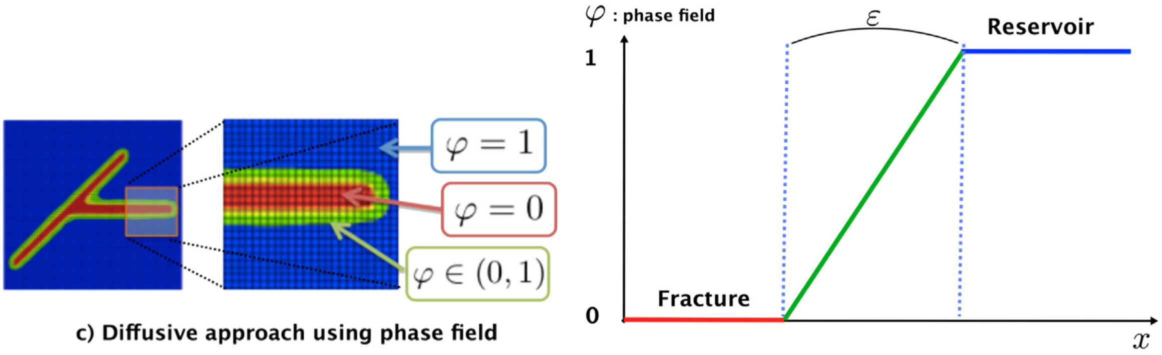

Fig. 2. Interpolation in the smooth transition zone.

been contributing numerous studies since 2013. The emphasis has been on rigorous mathematical modeling, physics-based discretizations, and numerical simulations. Computationally, a robust and efficient computational framework was developed resulting in IPACS — an integrated phase-field advanced crack propagation simulator. In this paper, we review and describe the main features of IPACS.

1.1. Definition and properties of phase-field modeling

The phase field model is a regularized approach based on the approximation of lower-dimensional surfaces and discontinuities to a volume as shown in Figs. 1 and 2. We denote the phase-field function by φ, where

$$\varphi = 0 \quad \text{on the fracture,}$$
$$\varphi = 1 \quad \text{in the intact material.}$$

The phase-field approach introduces a smooth transition zone between these two states. In more details: (A) represents the real fracture, (B) is the surface representation of the fracture, and (C) is the volume approximation of the fracture obtained using the phase field function, and in (D), the phase field function is illustrated with $\varphi = 0$ in the fracture, and $\varphi = 1$ in the bulk reservoir. The green zone in Fig. 1 indicates the diffusive zone with the length ε. This approximation is mathematically based on Γ-convergence; see for instance [3] and [4,5].

Advantages. Clearly, an appealing feature of phase-field is a variational continuum description that allows to adopt techniques from calculus of variations for the mathematical analysis and for which Galerkin techniques for the numerical discretization can be designed. With this variational description, the computation of curvilinear, complex crack patterns and networks can be achieved (see Fig. 3). Furthermore, nucleation, branching and merging and post processing of certain quantities such as stress intensity factors becomes redundant. Therefore, easy handling of fracture networks in possibly highly heterogeneous media can be treated.

With regard to numerical discretizations for fracture propagation in porous media, we list the following advantages and advancements. Phase-field fracture works on a fixed-grid topology that avoids expensive remeshing for resolving the exact fracture location; three-dimensional crack propagation can be easily implemented [6]. Adaptive schemes [7,8] and a parallel programming code [9,10] have been developed. Moreover, the phase-field

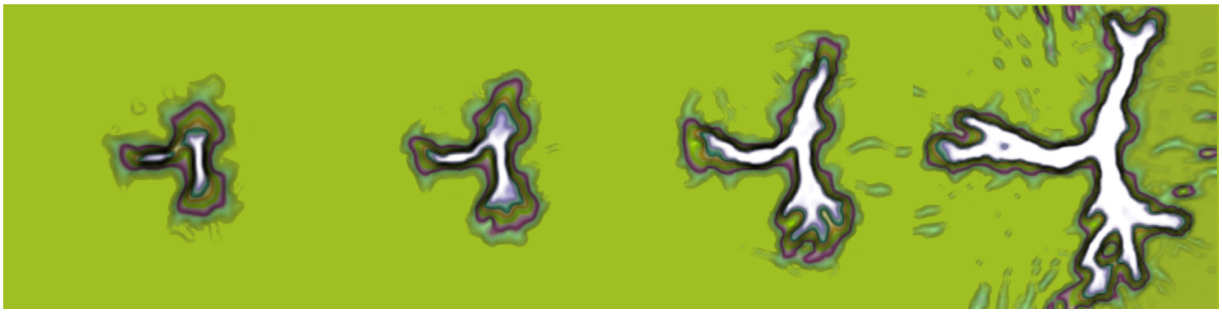

Fig. 3. Example of fracture propagation with a phase field model: snapshots at four different times of a propagating fracture.

variable can be used as an indicator function to formulate a pressure diffraction model for coupling with multiphysics phenomena [7,11,12]. Additionally, we can couple the phase field function with the field data (e.g probability map; [13]) and a reservoir simulator (e.g IPARS; [14,15]).

Shortcomings. On the other hand, since the diffusive transition zone tends to smear out the sharp crack surface and the characteristic length-scale parameter ε must be chosen appropriately, which is a modeling challenge for this approach in porous media [16,17]. For numerical treatment, an adaptive local grid refinement technique can be used to increase the crack surface resolution while keeping the computational costs low [7]. Moreover, the smeared interface makes it more difficult to describe interface conditions on the fracture boundary. For example, equations on the interface such as surfactants must be carefully derived and ideally must hold true in the sharp interface limit. Another challenge is the non-convex form of the underlying energy functional, resulting in slow convergence of numerical algorithms. A discussion of how these challenges have been met or are currently being addressed can be found in this paper.

1.2. Numerical modeling of fractures and industrial codes

Various numerical techniques for fracture propagation have been developed: XFEM/GFEM (extended/generalized) finite elements, boundary element methods (BEM), cohesive zone models, discrete fracture networks (DFN), extension to discrete deformable fracture networks (DDFN), and embedded discrete fracture models (EDFM), displacement-discontinuity methods, peridynamics, and phase-field. In industrial applications, to name a few, the following fracture stimulation codes are currently used: ResFrac, MFRAC, GOHFER, Kinetix. In the remainder of this paper, we concentrate on phase-field models.

1.3. Literature review on hydraulic phase-field fracture

Applying variational approaches, such as phase-field, to the simulation of propagation of pressurized fractures in an elastic medium was initiated in [18]. The pressurized fracture was described through a boundary term $\int_{\mathcal{C}} p[\mathbf{u}\cdot\mathbf{n}]$, with the crack $\mathcal{C}$ being a surface and $[\mathbf{u}\cdot\mathbf{n}]$ the displacement jump across the crack. The phase field handling of such terms goes back to [19].

In the years 2013 [20] and 2014 [21] (published in [22]), the first model for pressurized fractures in porous media (including Biot's coefficient α) was proposed and rigorously investigated. Here the displacement phase-field system was modeled in a monolithic framework. Later, a decoupled model was developed in [11] for which a corresponding robust numerical augmented Lagrangian (AL) approach was applied in [16]. We also refer to the theoretical development of a sharp interface model for pressurized fractures using variational techniques in [23]. The efficient and robust numerical solution of pressurized phase-field models based on quasi-monolithic approaches was presented in [6,7]. Based on the first models [20,21] (and also the current paper), fully monolithic solution techniques for pressurized fractures have been developed in [24,25]. For a different treatment of the decoupled model [11], using the discontinuous Galerkin (DG) formulation for the displacements, we refer to [26]. Various adaptive mesh refinement schemes for pressurized phase-field fracture, with focus on the crack path or other quantities of interest, have been proposed in [7–9].

The pressurized phase-field method has been further extended to fluid-filled fractures in which a Darcy equation is used for modeling fracture flow [12] and similar studies have appeared [27–29]. Rigorous mathematical analyses including detailed numerical studies of a fully-coupled fluid geomechanics phase-field model in porous media was first presented in [17]. Here, the important phenomenon of negative pressures at fracture tips was observed. This feature is known to appear in such configurations, but was not yet quantified using a phase-field method. In the year 2016, we note further contributions to fluid-filled phase-field fractures from [9,30,31] and more recently in [32]. To reduce the computational cost, we notice that parallel computation frameworks have been implemented in [7,9,18,28]. Local mesh adaptivity along with parallel computing was first implemented in [7] for two-dimensional problems and extended to three-dimensions in [6,9]. Coupling to other codes and reservoir simulators has been first accomplished in [15]. However, further research is necessary because the current modeling, the coupling algorithm, and the treatment of the multi-scale nature of the problem must be further improved such as in oil production, flow-backs and frac-hits.

Recent results concentrated on the extension to proppant flow [33], two-phase flow inside the fracture [34], single phase-flow for nonlinear poroelastic media [35], fractures in partially saturated porous media [36], fracture initialization with probability maps of fracture networks [13,37]. Consequences on further multiphysics coupling of the pressurized fractures interface law [38], more accurate crack width computations and computational analysis of fixed-stress splitting [39], a phase-field formulation (in elasticity) with a lower-dimensional lubrication formulation [40], and a multirate analysis in which different time steps for different regimes are used [41]. The extension to pressurized fractures and nonisothermal flow was undertaken in [42]. Several different boundary conditions were considered in [43], an optimal design using a genetic algorithm was proposed in [44], and interaction between natural and hydraulic fracture in [45]. Comparisons with experimental data were recently undertaken in [46]. The extension of porous media configurations for dynamic phase-field fracture was done in [47].

1.4. Time line and development stages of IPACS

Our references from the previous subsection are summarized in Fig. 4 showing the historical development of IPACS and indicating current developments as of the year 2019. The overall developments differ in the algorithms utilized for solving the phase-field, solid mechanics, and pressure (flow) systems. At the beginning, the solver for the constrained minimization problem for phase-field with irreversibility condition was a simple penalization technique. Shortly later in 2014 and 2015, the augmented Lagrangian and primal–dual active set approaches were added. A *stress-splitting* approach for the solid mechanics equations was implemented in 2015. Local mesh adaptivity and parallelization of the algorithms were added in [7,9], which then allowed us to address large scale computations. In fact, in these two papers, the core of IPACS was developed. In the years 2016–2018 several studies on the coupling algorithms for phase-field, solid mechanics, and pressure were developed and compared. Having this robust and efficient framework at hand, many different additional features were coupled to IPACS to illustrate the capability of our algorithms: proppant transport in the hydraulic fracture, constant temperature, initializing the natural fracture network with the probability map from the field data, coupling IPACS with the optimization algorithm for history matching and optimizing the fracture propagation are some selected examples. Ongoing further extensions are listed at the end of the conclusions.

1.5. Outline of this paper

The outline of this paper is as follows: In Section 2 we present the equations for modeling fracture propagation in porous media. Several extensions are recapitulated as well. In Section 3, we present physics-based discretization in time and space. Coupling algorithms, solvers and local mesh adaptivity are summarized in Section 4. In Section 5 representative numerical test scenarios are presented. The paper finishes with conclusions and acknowledgments to research funding.

2. Mathematical modeling of phase-field fractures in porous media

In our approach, the phase field model to predict the fracture propagation in porous media is based on the classical theory of [48]. Rewriting Griffith's model for brittle fractures in terms of a mechanics variational formulation was first accomplished in [49]. In [50] and [51,52], the authors refined modeling and material law assumptions to

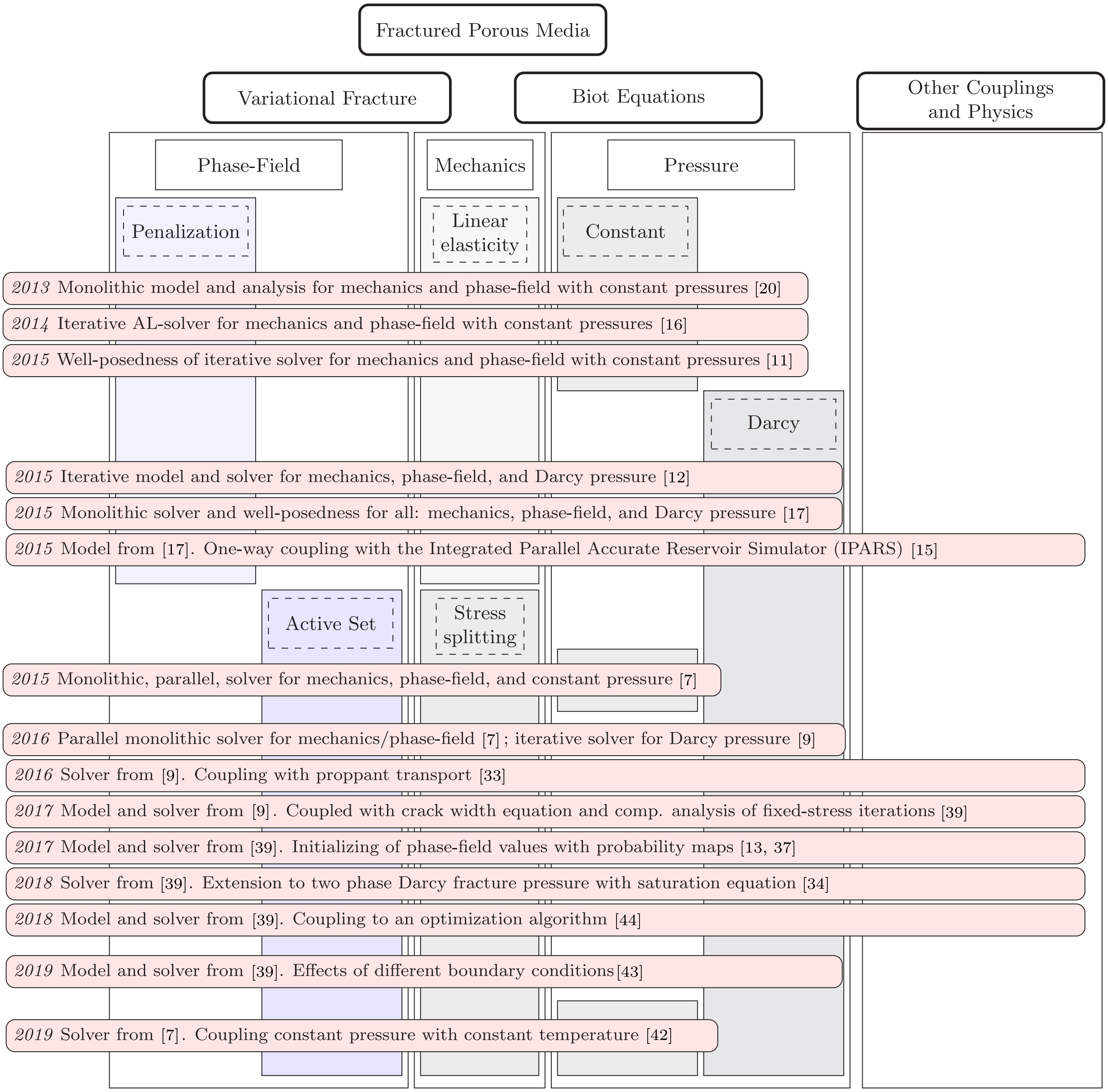

Fig. 4. Overview and timeline of the development of IPACS. The background tables indicate the features for each published manuscript. For example, the item *2013* Monolithic model and analysis for mechanics and phase-field with constant pressures [20] includes penalization technique for the phase-field system, linear elasticity without splitting for mechanics, and constant pressure for the flow.

formulate an incremental thermodynamically consistent phase-field model for fracture propagation. These studies are the starting point for our formulation of a *phase-field fracture approach in porous media*. As indicated in Fig. 4, two research fields must be joined: fractured geomechanics and flow in porous media. In this section, we describe our current models and equations.

2.1. Notation

Let $\Lambda \in \mathbb{R}^d$ $(d = 2, 3)$ be a smooth open and bounded computational domain with Lipschitz boundary $\partial\Lambda$ and let $I := (0, T]$ be the time interval with the end time value $T > 0$. The (lower-dimensional) fracture is described by $\mathcal{C} \in \mathbb{R}^{d-1}$.

2.2. Phase-field modeling in elasticity

Before we tackle phase-field descriptions in poro-elasticity, we recapitulate the main features of phase-field in elasticity.

2.2.1. Constitutive modeling of geomechanics

The displacement of the solid, $\mathbf{u}(\mathbf{x},t) : \Omega \times I \to \mathbb{R}^d$, $0 \le t \le T$, is modeled in the classical linear elastic, homogeneous, and isotropic solid domain $\Omega = \Lambda \backslash \bar{\mathcal{C}}$. The linear momentum in the solid is given as

$$-\nabla \cdot \sigma(\mathbf{u}) = \rho \mathbf{g} \quad \text{in } \Omega \times I, \tag{1}$$

where, $\sigma = \sigma(\mathbf{u})$ is the elastic stress tensor,

$$\sigma(\mathbf{u}) = 2\mu \mathbf{e}(\mathbf{u}) + \lambda \operatorname{tr}(\mathbf{e}(\mathbf{u}))I,$$

and $e(\mathbf{u})$ is the symmetric strain tensor defined as

$$\mathbf{e}(\mathbf{u}) := \frac{1}{2}\left(\nabla \mathbf{u} + \nabla \mathbf{u}^T\right).$$

Here ρ is the mass density, $\mathbf{g}$ the gravity, μ and λ are Lamé coefficients, and I is the identity tensor. Next, we introduce the Francfort–Marigo functional, which describes the energy of a crack in an elastic medium as

$$E(\mathbf{u}, \mathcal{C}) = \frac{1}{2}\int_\Omega \sigma(\mathbf{u}) : \mathbf{e}(\mathbf{u}) + G_c H^{d-1}(\mathcal{C}). \tag{2}$$

The Hausdorff measure $H^{d-1}(\mathcal{C})$ denotes the length of the crack and is multiplied by a fracture toughness $G_c > 0$, that is considered in fracture mechanics to be the critical energy release rate.

We describe the continuous phase field function $\varphi : \Lambda \times I \to [0,1]$ where $\varphi(\mathbf{x},t) = 0$ in the crack region and $\varphi(\mathbf{x},t) = 1$ in the unbroken material. This introduces a diffusive transition zone, with a length given by the regularization parameter $\varepsilon > 0$. See Fig. 1(D) for details. Employing the phase field to describe the fracture, we consider the global constitutive dissipation functional and obtain (see e.g., [53])

$$E_\varepsilon(\mathbf{u},\varphi) = \int_\Lambda \frac{1}{2} g_D(\varphi)\sigma(\mathbf{u}) : \mathbf{e}(\mathbf{u})\, d\mathbf{x} + G_c \int_\Lambda \left(\frac{1}{2\varepsilon}(1-\varphi)^2 + \frac{\varepsilon}{2}(\nabla\varphi)^2\right) d\mathbf{x}, \tag{3}$$

with the degradation function $g_D(\varphi) := (1-\kappa)\varphi^2 + \kappa$ with κ being a small positive regularization parameter.

Remark 2.1 (*Choice of ε and κ in Practice*)**.** In our numerical simulations shown in Section 5, we choose $\varepsilon = 2h_{min}$, where h_{min} is the minimum spatial discretization parameter. The choice of ε versus the spatial discretization parameter h is mathematically more delicate because of the Γ-convergence theories [5,54]. Computational tests with different relations between ε and h were carried out in [7,8]. In addition, $\kappa = 10^{-12}$ in our computations, and choosing small enough κ was suggested in [53].

Since the energy degradation only acts on the tensile part, the stress tensor is decomposed into a tensile part $\sigma^+(\mathbf{u})$ and a compressive part $\sigma^-(\mathbf{u})$ by [50][1]

$$\sigma^+(\mathbf{u}) := (\frac{2}{d}\mu + \lambda)tr^+(e(\mathbf{u}))I + 2\mu(e(\mathbf{u}) - \frac{1}{d}tr(e(\mathbf{u}))I), \tag{4}$$

$$\sigma^-(\mathbf{u}) := (\frac{2}{d}\mu + \lambda)tr^-(e(\mathbf{u}))I, \tag{5}$$

where

$$tr^+(e(\mathbf{u})) = \max(tr(e(\mathbf{u})), 0), \quad tr^-(e(\mathbf{u})) = tr(e(\mathbf{u})) - tr^+(e(\mathbf{u})). \tag{6}$$

---

[1] We note that there exist a series of other stress/strain energy splitting laws. A comparison for phase-field in elasticity between some of them was provided in [55] and more recently in [56]. All these laws have their advantages and shortcomings and are subject to further research in mechanics.

Finally, we rewrite (3) to obtain

$$E_\varepsilon(\mathbf{u},\varphi) = \int_\Lambda \frac{1}{2} g_D(\varphi)\sigma^+(\mathbf{u}) : \mathbf{e}(\mathbf{u})\, d\mathbf{x} + \int_\Lambda \frac{1}{2}\sigma^-(\mathbf{u}) : \mathbf{e}(\mathbf{u})\, d\mathbf{x} + G_c \int_\Lambda \left(\frac{1}{2\varepsilon}(1-\varphi)^2 + \frac{\varepsilon}{2}(\nabla\varphi)^2\right) d\mathbf{x}. \tag{7}$$

2.2.2. Crack irreversibility constraint

A crucial assumption is the crack irreversibility; namely that a cracked material cannot heal. Mathematically, we express irreversibility through a variational inequality in time:

$$\varphi \le \varphi^{old}, \tag{8}$$

This yields several challenges: first, the functional (7) becomes a constraint problem. Second, the constraint must be incorporated in the model, yielding a further nonlinearity. Third, this nonlinearity must be numerically realized. Fourth, the geomechanics equation is quasi-static without any explicit time derivatives, but the constraint is now a time-dependent term.

2.2.3. Boundary conditions

The system is supplemented with initial and boundary conditions. The initial condition for the phase field function is given by $\varphi(\mathbf{x},0) = \varphi^0$ for all $\mathbf{x} \in \Lambda(t=0)$, where φ^0 is a given smooth initial fracture. The boundary $\partial\Lambda$ is decomposed into two non-overlapping components $\partial\Lambda = \overline{\partial\Lambda_D} \cup \overline{\partial\Lambda_N}$ with $\partial\Lambda_N \cap \partial\Lambda_D = \emptyset$. For the displacement $\mathbf{u}$, we prescribe Dirichlet boundary condition on Λ_D and homogeneous Neumann boundary condition on Λ_N. For the phase field function, we prescribe homogeneous Neumann conditions on $\partial\Lambda$. This system is based on a quasi-stationarity assumption in which the time enters through time-dependent boundary conditions as a load parameter or right hand side sources,

2.3. Phase-field modeling with the biot system for poro-elasticity

The energy functional described in the previous section is now extended to fractured porous media by employing Biot's theory [57,58]. To this end, we extend the functional (7) to (see [20,22]):

Formulation 2.2 (*Phase-field Fracture in porous Media - Mechanics Step*)**.** *Let the pressure* $p(\mathbf{x},t) : \Omega \times I \to \mathbb{R}$, $0 \le t \le T$ *be given. Find* $\mathbf{u} : \Lambda \times I \to \mathbb{R}^d$ *and* $\varphi : \Lambda \times I \to \mathbb{R}$ *such that*

$$\begin{aligned} E_\varepsilon(\mathbf{u},p,\varphi) = &\int_\Lambda \frac{1}{2} g_D(\varphi)\sigma(\mathbf{u}) : e(\mathbf{u})\, dx - \int_{\partial\Lambda} \tau\cdot\mathbf{u}\, dS \\ &- \int_\Lambda (\alpha-1)\varphi^2 p\nabla\cdot\mathbf{u}\, dx + \int_\Lambda (\varphi^2\nabla p)\mathbf{u}\, dx \\ &+ G_c\int_\Lambda \left(\frac{1}{2\varepsilon}(1-\varphi^2) + \frac{\varepsilon}{2}|\nabla\varphi^2|\right) dx, \\ \varphi \le \varphi^{old} \quad &in\ \Lambda\times I, \\ \varphi(0) = \varphi_0 \quad &in\ \Lambda\times\{t=0\}, \end{aligned}$$

where $\alpha \in [0,1]$ *is the Biot coefficient. If* $\alpha = 0$*, we refer to the constant pressure as the pressurized fracture regime. If* $\alpha \neq 0$*, we solve for the pressure and refer to this case as the fluid-filled fracture regime. For typical parameters, we refer to Table 1.*

Remark 2.3. The mathematical analysis of $E_\varepsilon(\mathbf{u},p,\varphi)$ was established in [20,22] for a monolithic formulation and in [11] for a decoupled approach. Therein, cut-off functions for φ were used that are omitted in this paper.

Remark 2.4. In practice, we solve $E_\varepsilon(\mathbf{u},p,\varphi)$ by computing the stationary points using the first-order optimality conditions, which result in the so-called Euler–Lagrange equations, i.e., two PDEs for $\mathbf{u}$ and φ. These relationships are classic and well-known. For phase-field fracture, we refer the reader again to [7,11,20,22].

Table 1
Unknowns and effective coefficients with units.

	Quantity	Unity
K_R	Permeability of the poroelastic domain	Darcy
K_F	Fracture permeability	Darcy
ρ_b	Bulk density	kg/m^3
ρ_F	Reference state fracture fluid density	kg/m^3
ρ_R	Reference state pore fluid density	kg/m^3
η_F	Fracture fluid viscosity	kg/m s
η_R	Pore fluid viscosity	kg/m s
α	Biot's coefficient	–
M	Biot's modulus	Pa
c_F	Fracture fluid compressibility	1/Pa
$\mathbf{g}$	Gravity	m/s^2

2.4. Coupling single-phase flow using a diffraction system

In the previous section, we have addressed the mechanics step of phase-field fracture in porous media. The current section is devoted to the *flow step*. In a non-fractured classical Biot system the flow equation is of parabolic type. Our principal design decision is to consider the fracture flow equation to be of the same type. Consequently, both flow equations can be combined to *one single equation*.

This yields a so-called generalized parabolic system [59], or diffraction system [60], in which a parabolic equation is used and its coefficients change in time and space. In the following, we recall the main steps from [12].

In more details, the flow equation in porous media comes from the quasi-static Biot equations (see e.g. [58]) that reads as follows:

$$\partial_t\Big(\frac{1}{M}p_R + \nabla\cdot(\alpha\mathbf{u})\Big) + \nabla\cdot\Big(\frac{K_R}{\eta_R}(\rho_R\mathbf{g} - \nabla p_R)\Big) = \frac{q_R}{\rho_R}. \tag{9}$$

In case of a fluid-filled fracture, lubrication theory is applied to describe the fluid flow (see e.g. [2,61–63]); namely one replaces the moving boundary Stokes flow by a Reynolds equation. Our derivations of such lubrication laws can be found in [12,34].

However in our work fractures propagate in a poroelastic medium. Therefore, their description is obtained by upscaling the fluid–structure pore scale first principle equations. In this new setting the meaning of a Griffith's type surface energy is not clear and we choose to deal with a physical three-dimensional fracture, to which we can attribute an energy term leading to propagation [11,17]. Detailed discussions of our choice to consider the lower-dimensional fracture as a three-dimensional object can be found in [17][Section 2.1 and 2.4].

2.4.1. Quasi-Newtonian flow

In the crack, we consider incompressible viscous flow. Since this takes place in a thin domain, we replace the Navier–Stokes equations by the appropriate three-dimensional Darcy law. Its derivation, and in particular the permeability calculation, is based on the lubrication approximation (see [64]). In the case of Newtonian incompressible viscous flow in the crack $\mathcal{C}$, the three-dimensional Darcy law using lower dimensional lubrication approximation is derived in [12].

We now turn to the description of the fracture pressure equation where we assume the fracturing fluid is quasi-Newtonian. The motivation is that the fluid rheology changed by polymers allows for larger fracture apertures due to the transport of the proppant.

We use the following density–pressure relationship

$$\rho_F = \rho_F^0 \exp(c_F(p_F - p_F^0)) \approx \rho_F^0[1 + c_F(p_F - p_F^0)],$$

where ρ_F^0 denotes the (constant) reference density, $p_F : \Omega \times I \to \mathbb{R}$ is the fluid fracture pressure (Pa), and p_F^0 is a given initial fluid fracture pressure. The fluid compressibility c_F is assumed to be small and $\rho_F \approx \rho_F^0$. Nevertheless, even after linearization, compressibility effects are important in the pressure equation. With small c_F, the fracture mass conservation equation is given by:

$$c_F \partial_t p_F + \nabla \cdot (\mathbf{v}_F) = \frac{q_F}{\rho_F^0} \quad \text{in } \mathcal{C} \times I, \tag{10}$$

where q_F is a source term and $\mathbf{v}_F$ is nonlinear Darcy's law defined below.

Relative velocity satisfies nonlinear Darcy's law

$$\mathbf{v}_F = \frac{K_F}{\eta_F^{1/m}} |\mathbf{f} - \nabla p_F|^{\frac{1}{m}-1} (\mathbf{f} - \nabla p_F) + (0, 0, v_L). \tag{11}$$

When $m = 1$ the fluid is slick water.

2.4.2. *Pressure diffraction system*

In order to formulate the flow equations in the reservoir and the fracture, respectively, we employ the phase field function as an indicator function.

We denote by $\Omega_F(t)$ and $\Omega_R(t)$ the open subsets of the space–time domain $\Lambda \times I$ at time t. $\Omega_R(t)$ is filled with the unbroken material (reservoir domain). In the approximation, the fracture is approximated by a volume term and $\mathcal{C}$ becomes $\Omega_F(t)$. Thus, we define $\partial\mathcal{C} := \Gamma(t) := \bar{\Omega}_F(t) \cap \bar{\Omega}_R(t)$. Following the above derivation we obtain

$$\rho_R \partial_t (\frac{1}{M} p_R + \alpha \nabla \cdot \mathbf{u}) - \nabla \cdot \frac{K_R \rho_R}{\eta_R} (\nabla p_R - \rho_R \mathbf{g}) = q_R \quad \text{in} \quad \Omega_R(t) \times I, \tag{12}$$

$$\rho_F \partial_t (c_F p_F) - \nabla \cdot \frac{K_F \rho_F}{\eta_F} (\nabla p_F - \rho_F \mathbf{g}) = q_F - q_L \quad \text{in} \quad \Omega_F(t) \times I. \tag{13}$$

Using an indicator function, we can easily combine both equations. Thus, we obtain one slightly compressible Darcy equation, but with varying coefficients:

Formulation 2.5 (*Pressure Diffraction Equation - Flow Step; Phase-field in Porous Media*)**.** *Set* $\chi_R(\cdot, t) = 1$ *for* $x \in \Omega_R(t)$ *and* $\chi_F(\cdot, t) = 1 - \chi_R(\cdot, t)$ *for* $x \in \Omega_F(t)$. *Then, we have: Find* $p : \Omega \times I \to \mathbb{R}$ *such that*

$$\rho \partial_t (cp) + \chi_R \rho \partial_t (\alpha \nabla \cdot u) - \nabla \cdot K_{eff} (\nabla p - \rho g) = q \quad \text{in} \quad \Lambda(t) \times I,$$

with $p = p_R$ *in* $\Omega_R(t)$ *and* $p = p_F$ *in* $\Omega_F(t)$ *and the temporally and spatially varying coefficients:*

$$\begin{aligned} \rho &:= \chi_R \rho_R + \chi_F \rho_F, \\ c &:= \chi_R \frac{1}{M} p_R + \chi_F c_F, \\ K_{eff} &:= \chi_R \frac{K_R \rho_R}{\eta_R} + \chi_F \frac{K_F \rho_F}{\eta_F}, \\ q &:= \chi_R q_R + \chi_F (q_F - q_L). \end{aligned}$$

Remark 2.6. We notice that the indicator functions $\chi_R(\cdot, t)$ and $\chi_F(\cdot, t)$ are introduced formally here. The concrete realization is explained in Section 3.3. Specifically, therein we use the phase-field variable φ to determine $\chi_R(\cdot, t)$ and $\chi_F(\cdot, t)$. To this end, the indicator variables vary smoothly from $\chi_R(\cdot, t) = 1$ for $x \in \Omega_R(t)$ to $\chi_F(\cdot, t) = 1 - \chi_R(\cdot, t)$ for $x \in \Omega_F(t)$.

For the fracture flow, we adopt a three-dimensional lubrication equation [12]. Inside this function, the fracture permeability is assumed to be isotropic such that

$$K_F = \frac{1}{12} w(\mathbf{u})^2,$$

where $w(\mathbf{u}) = [\mathbf{u} \cdot \mathbf{n}]$ denotes the aperture (width) of the fracture, which means that the jump $[\cdot]$ of normal displacements has to be computed.

Definition 2.7 (*Phase-field Fracture in Porous Media*)**.** Combining the PDEs for solving $(\mathbf{u}, \varphi)$ in the mechanics step in Formulation 2.2 (see also Remark 2.4) and the flow step for solving p in Formulation 2.5 is called the *phase-field fracture in porous media*.

2.5. Proppant transport in fracture propagation

In this section, we extend the phase-field framework to account for proppant transport inside the fracture. This work was presented in [33]. For modeling the proppant transport we solve an advective equation that determines the volumetric distribution of concentration c, see e.g., [2,65].

Formulation 2.8. *Find the concentration $c : \Lambda \times I \to \mathbb{R}$ such that for all times $t \in I$:*

$$\partial_t(\varphi^\star c) + \nabla \cdot (\mathbf{v}_p c) = Q c_q \frac{q_F}{\rho_F}, \quad \text{in } \Lambda(t) \times I, \tag{14}$$

where $\varphi^\star$ is the porosity, $\mathbf{v}_p = Q\mathbf{v}$, $Q > 0$ is a coefficient for the velocity, and $\mathbf{v}$ is obtained from the pressure system. The initial condition is given by

$$c(\mathbf{x}, 0) = c_0(\mathbf{x}), \quad \forall \mathbf{x} \in \Lambda,$$

where c is the species concentration advected, c_q is a general source or sink term. As boundary conditions, we prescribe

$$\mathbf{v}_p \cdot \mathbf{n} = 0 \quad \text{on } \partial\Lambda \times I.$$

We note that various types of proppant velocity models based on theoretical and experimental results with careful assumptions for proppant particle size, density, fracture width and fluid velocity have been derived in previous studies [2,66–74]. For example, the velocity $\mathbf{v}_p = Q\mathbf{v} - (1-c)\mathbf{v}_s)$ is discussed by regarding the slip velocity vector ($\mathbf{v}_s$) with settling of proppant. The choice of a model for $\mathbf{v}_p$ is non-trivial since each has different assumptions with varying results. Therefore, in our current framework, we focus on a prototype model to observe the distribution of proppant in the fracture. We assume the proppant velocity is equal to the fluid velocity (no slip and settling) and instead of providing any specific Q, we restrict Q to be a constant.

2.6. Two-phase flow in the fracture

In this final extension, a two-phase flow model for fracture flow is derived. In our global systems, we have two variables for the saturation in a fracture denoted by $s_{F,\mathrm{inj}}$ (the saturation for the injection fluid) and $s_{F,\mathrm{res}}$ (saturation for the residing fluid), and three variables for the pressure denoted by p_R, $p_{F,\mathrm{inj}}$, $p_{F,\mathrm{res}}$, where p_R is the pressure for the reservoir, $p_{F,\mathrm{res}}$ is the pressure for residing fluid in a fracture and $p_{F,\mathrm{inj}}$ is the pressure for the injection fluid in a fracture. However after employing the relation

$$s_{F,\mathrm{inj}} + s_{F,\mathrm{res}} = 1, \quad \text{and} \quad p_c = p_{F,\mathrm{res}} - p_{F,\mathrm{inj}}, \tag{15}$$

where p_c is referred as the capillary pressure in a fracture, we only solve for the saturation and the pressure of the injecting fluid, $s_{F,\mathrm{inj}}$, $p_{F,\mathrm{inj}}$ in a fracture.

In the reservoir, we have p_R, but a saturation variable is not defined since we assume a single phase fluid in the reservoir. Thus, we obtain the following:

Formulation 2.9. *Find $s_{F,inj}$ such that*

$$\partial_t(\varphi^\star_F s_{F,inj}) - \nabla \cdot \left(K_F \frac{k_{F,inj}(s_{F,inj})}{\eta_{F,inj}} \nabla p_{F,inj} \right) = q_{F,inj} \quad \text{in } \Omega_F \times I, \tag{16a}$$

$$K_F \frac{k_{F,inj}(s_{F,inj})}{\eta_{F,inj}} \nabla p_{F,inj} \cdot \mathbf{n}_F = 0 \quad \text{on } \Gamma_F(t) \times I, \tag{16b}$$

where $\varphi^\star_F$ is the porosity of the fracture which is set to one, and $\eta_{F,res}$, $\eta_{F,inj}$, are the viscosities for each fluid, respectively. Moreover, $q_{F,inj} := \tilde{s}_{F,inj}\tilde{q}_{F,inj}$, where $\tilde{s}_{F,inj}$, $\tilde{q}_{F,inj}$ are the saturation injection/production terms and flow injection/production, respectively. If $\tilde{q}_{F,inj} > 0$, $\tilde{s}_{q,inj}$ is the injected saturation of the fluid and if $\tilde{q}_{F,inj} < 0$, $\tilde{s}_{q,inj}$ is the produced saturation. We note that $\tilde{s}_{q,inj} + \tilde{s}_{q,res} = 1$.

In addition, find the pressure $p_{F,inj}$ such that

$$-\nabla \cdot \left(K_F \lambda_{tot} \nabla p_{F,inj} + K_F \lambda_{F,res} \nabla p_c(s_{F,inj}) \right) = (q_F)_{tot} \quad \text{in } \Omega_F(t) \times I, \tag{17}$$

Here the total mobility, the mobility for the injecting fluid, and the mobility for the residing fluid, are defined respectively:

$$\lambda_{tot} := \lambda_{tot}(s_{F,inj}) = \lambda_{F,inj}(s_{F,inj}) + \lambda_{F,res}(s_{F,inj}), \tag{18a}$$

$$\lambda_{F,inj} := \lambda_{F,inj}(s_{F,inj}) = \frac{k_{F,inj}(s_{F,inj})}{\eta_{F,inj}}, \tag{18b}$$

$$\lambda_{F,res} := \lambda_{F,res}(s_{F,inj}) = \frac{k_{F,res}(s_{F,inj})}{\eta_{F,res}}, \tag{18c}$$

$$\text{and} \quad (q_F)_{tot} := q_{F,inj} + q_{F,res}. \tag{18d}$$

The above formulation is similar to the two phase flow model in porous media as discussed in [75–79]; here we have computed new relative permeabilities and employed a capillary pressure for modeling two phase flow in the fracture.

2.7. Fracture opening displacement

In the displacement phase-field system, the width of the fracture is not explicitly defined. For accurate width computations of non-planar fractures an additional algorithm is required. Formally the definition of the width reads:

$$2w := 2w(\mathbf{u}) = 2h = -[\mathbf{u} \cdot \mathbf{n}_F],$$

which is the jump of the normal displacements, where $\mathbf{n}_F$ is the unit normal on the crack surface (Γ_F).

The phase-field variable creates isolines that can be used to define the normal vector as usually done in level-set methods:

Definition 2.10. The normal vector is defined as:

$$\mathbf{n}_F := \frac{\nabla \varphi_{LS}}{\|\nabla \varphi_{LS}\|}$$

Then, we obtain:

$$2w = -[\mathbf{u} \cdot \mathbf{n}_F] = -2\mathbf{u} \cdot \frac{\nabla \varphi_{LS}}{\|\nabla \varphi_{LS}\|},$$

by approximating the normal vector on the crack surface (Γ_F) with the level set values φ_{LS} of a specific isoline of the fracture. To compute φ_{LS}, we proceed as follows: Let Γ_F be the fracture interface. We now define Γ_F as the zero level-set of a function φ_{LS} such that

$$\begin{aligned} \varphi_{\mathsf{LS}} &> 0, \quad \mathbf{x} \in \Omega_R, \\ \varphi_{\mathsf{LS}} &< 0, \quad \mathbf{x} \in \Omega_F, \\ \varphi_{\mathsf{LS}} &= 0, \quad \mathbf{x} \in \Gamma_F, \end{aligned}$$

where the isoline φ_{LS} is obtained from the phase-field variable φ by

$$\varphi_{LS} := \varphi - C_{LS}. \tag{19}$$

Here, $C_{LS} \in (0, 1)$ is a constant selected for approximating the fracture boundary Γ_F. Throughout this paper for simplicity, we set $C_{LS} = 0.5$. Thus, $\Gamma_F := \{\mathbf{x} \in \Lambda \mid \varphi(\mathbf{x}, t) = C_{LS}\}$, $\Omega_R := \{\mathbf{x} \in \Lambda \mid \varphi(\mathbf{x}, t) > C_{LS}\}$ and $\Omega_F := \{\mathbf{x} \in \Lambda \mid \varphi(\mathbf{x}, t) < C_{LS}\}$. Details of the entire procedure and underlying motivation are provided in [39,80].

Formulation 2.11 (*Level-set Values Obtained from Phase-field*)**.** *As second alternative approach, the level-set values are immediately obtained from the phase-field by:*

$$\varphi_{\mathsf{LS}} = \varphi - C_{LS}.$$

Formulation 2.12 (*Computing the Width with the Normal Vector on the Fracture Boundary Γ_F*)**.** *Under the assumption that $\mathbf{u}^+ \cdot \mathbf{n} = -\mathbf{u}^- \cdot \mathbf{n}$ (symmetric displacements at the fracture boundary), we compute the width* *locally in each quadrature point*

$$w_D := 2\mathbf{u} \cdot \mathbf{n}_F = -2\mathbf{u} \cdot \frac{\nabla \varphi_{LS}}{\|\nabla \varphi_{LS}\|} \quad \text{on } \Gamma_F. \tag{20}$$

Here we assume that $\mathbf{u}^+ \cdot \mathbf{n} = -\mathbf{u}^- \cdot \mathbf{n}$, *which has been justified for tensile stresses and homogeneous isotropic media.*

Formulation 2.13 (*Crack Width Interpolation Inside the Fracture*)**.** *We solve the following width-problem: Find* $w : \Lambda \to \mathbb{R}$ *such that*

$$\begin{aligned} -\Delta w &= \beta \|w_D\|_{L^\infty(\Lambda)} && \text{in } \Lambda, \\ w &= w_D && \text{on } \Gamma_F, \\ w &= 0 && \text{on } \partial\Lambda, \end{aligned}$$

where $\beta > 0$ *in order to obtain a smooth parabola-type width-profile in the fracture. We note that* β *is problem-dependent and heuristically chosen.*

3. Numerical discretization

We discuss the discretization in time and space. An emphasis is on physics-based discretizations respecting conservation laws such as local mass conservation. From the presented overall governing system, we can currently solve in IPACS for up to six unknowns. Thanks to the modular structure of the implementation, more physical unknowns can be added in future extensions.

Currently, we solve for displacements $\mathbf{u}$, phase-field φ, pressure p, concentration of the proppant c, saturation for two phase flow s, and the width w. In order to ensure physics-based discretizations, we discretize these variables according to their conservation properties.

3.1. Temporal discretization

The partition of the time interval is defined as

$$0 = t_0 < t_1 < \cdots < t_n < \cdots < t_N = T,$$

where $N \in \mathbb{N}$ denotes the total number of time steps. Time derivatives in IPACS are usually discretized with a standard finite difference quotient. For instance, the phase-field inequality constraint $\partial_t \varphi$ is discretized via

$$\partial_t \varphi^n = \frac{\varphi^n - \varphi^{n-1}}{\Delta t}$$

where $\varphi^n := \varphi(t_n)$ and $\Delta t = t_n - t_{n-1}$ denotes the time step size. For time-dependent equations as pressure, saturation, and proppant, the other terms are taken at the current time point t_n in order to have implicit schemes that enjoy better numerical stability in comparison to explicit schemes.

3.2. Physics-based spatial discretization

For the spatial discretization of all the system described above, we employ Galerkin finite element methods. An emphasis is on physics-based discretizations respecting conservation laws such as local mass conservation. Thus, not only classical continuous Galerkin finite element methods are utilized, but also enriched Galerkin finite element is employed to ensure local mass conservation.

The notations for spatially-discretized variables after the finite element discretization are denoted by

$$\mathbf{U}(\cdot, t), \ \Phi(\cdot, t), \ P(\cdot, t), \ W(\cdot, t), \ C(\cdot, t), \ S(\cdot, t) \tag{21}$$

for the displacements $\mathbf{u}(\cdot, t)$, phase-field $\varphi(\cdot, t)$, pressure $p(\cdot, t)$, crack-width $w(\cdot, t)$, proppant concentration $c(\cdot, t)$, and saturation $s(\cdot, t)$, respectively. Then we combine the temporal and spatial discretizations, and we denote the approximation of the solution variables at the given time point t_n

$$\mathbf{U}(\cdot, t_n), \ \Phi(\cdot, t_n), \ P(\cdot, t_n), \ C(\cdot, t_n), \ S(\cdot, t_n), \ W(\cdot, t_n), \tag{22}$$

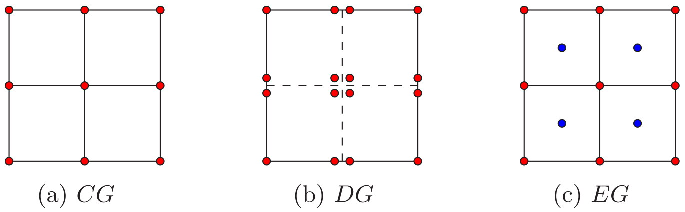
(a) *CG* (b) *DG* (c) *EG*

Fig. 5. Comparison of the degrees of freedom for a two-dimensional Cartesian grid ($\mathbb{Q}^1$) with linear CG, DG, and, EG approximations. Here the node in the middle of the grid at (c) indicates a piece-wise constant.

by

$$\mathbf{U}^n,\ \Phi^n,\ P^n,\ C^n,\ S^n,\ W^n, \tag{23}$$

for $0 \le n \le N$.

3.2.1. A continuous Galerkin finite element method

We consider a mesh family $\{\mathcal{T}\}$ and we assume that each mesh $\mathcal{T}$ is a subdivision of $\bar{\Lambda}$ made of disjoint elements $\mathcal{K}$, i.e., squares when $d = 2$ or cubes when $d = 3$. Each subdivision is assumed to exactly approximate the computational domain, thus $\bar{\Lambda} = \cup_{\mathcal{K}\in\mathcal{T}}\mathcal{K}$. The diameter of an element $\mathcal{K} \in \mathcal{T}$ is denoted by h and we denote $h_{\min}$ for the minimum. For any integer $k \ge 1$ and any $\mathcal{K} \in \mathcal{T}$, we denote by $\mathbb{Q}^k(\mathcal{K})$ the space of scalar-valued multivariate polynomials over $\mathcal{K}$ of partial degree of at most k. The vector-valued counterpart of $\mathbb{Q}^k(\mathcal{K})$ is denoted $\mathbf{Q}^k(\mathcal{K})$.

First, the spatial approximation of $W(\cdot, t)$ is approximated by using continuous piecewise polynomials given in the continuous Galerkin finite element space,

$$\mathbb{W}(\mathcal{T}) := \{W \in C^0(\bar{\Lambda};\mathbb{R}) \mid W|_{\mathcal{K}} \in \mathbb{Q}^1(\mathcal{K}), \forall\mathcal{K} \in \mathcal{T}\}. \tag{24}$$

The other choice for the finite element space of pressure equation to ensure the local conservative mass is discussed in next section. The spatially discretized solution variables for displacement and phase-field are approximated in $\mathbf{U} \in \mathcal{C}^1([0,T];\mathbb{V}_0(\mathcal{T}))$ and $\Phi \in \mathcal{C}^1([0,T];\mathbb{Z}(\mathcal{T}))$, where

$$\mathbb{V}_0(\mathcal{T}) := \{W \in C^0(\bar{\Lambda};\mathbb{R}^d) \mid W = \mathbf{0} \text{ on } \partial\Lambda, W|_{\mathcal{K}} \in \mathbf{Q}^1(\mathcal{K}), \forall\mathcal{K} \in \mathcal{T}\}, \tag{25}$$

$$\mathbb{Z}(\mathcal{T}) := \{Z \in C^0(\bar{\Lambda};\mathbb{R}) \mid Z^{n+1} \le Z^n \le 1, Z|_{\mathcal{K}} \in \mathbb{Q}^1(\mathcal{K}), \forall\mathcal{K} \in \mathcal{T}\}. \tag{26}$$

3.2.2. A locally conservative enriched Galerkin finite element method

When the pressure (flow) equation is coupled with the two transport problems for proppant transport or saturation for two-phase flow, it is crucial to employ sophisticated spatial discretizations, ensuring locally conservative fluxes. Thus, for the pressure system, we employ the enriched Galerkin (EG) finite element method, that was first proposed in [81] and was extended in [79,82–84]. Using EG in mechanics was proposed in [85].

One of the most popular and successful methods in terms of the local flux conservation is the discontinuous Galerkin (DG) finite element method; see e.g. [86]. DG can deal robustly with general partial differential equations as well as with equations whose type changes within the computational domain such as from advection dominated to diffusion dominated. They are naturally suited for multiphysics applications (for instance recent applications of black-oil models in porous media [87]), and for problems with highly varying material properties. However, several disadvantages in the use of the DG are that the method is computationally costly due to the number of degrees of freedom.

The Enriched Galerkin finite element method (EG) is constructed by enriching CG (continuous Galerkin) with piecewise constant functions; see Fig. 5. The several advantages of EG include local flux conservation with fewer degrees of freedom than that of DG, treatment of non-matching grids, and a fast effective solver for elliptic and parabolic problems. In addition, one is not required to enrich the entire computational domain but only those subdomains that require local conservation.

The EG space approximation is utilized for both $P(\cdot,t)$ and $S(\cdot,t)$, the pressure and saturation functions, respectively. Those are approximated by piecewise polynomials in

$$\mathbb{V}^{EG}(\mathcal{T}) := M_0^k(\mathcal{T}) + M^0(\mathcal{T}), \tag{27}$$

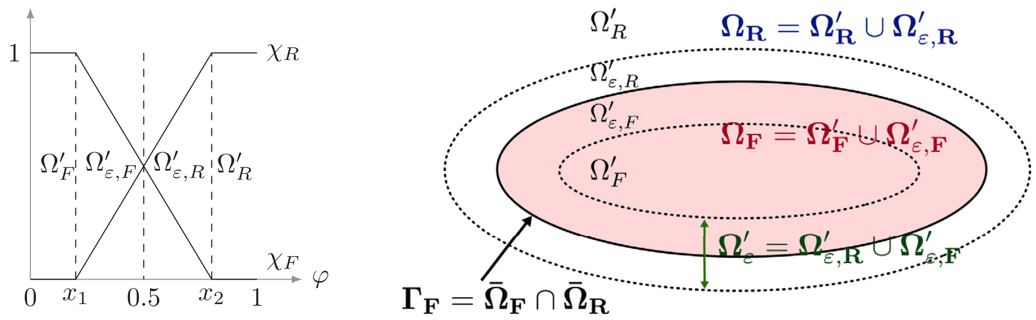

(a) (b)

Fig. 6. (a) The linear indicator functions χ_F and χ_R illustrated with adjustable constants x_1 and x_2. This is an example for the case where $C_{LS} = 0.5$. (b) Definitions for different domains are illustrated. Here, $\Omega_F := \Omega'_F \cup \Omega'_{\varepsilon,F}$ and $\Omega_R := \Omega'_R \cup \Omega'_{\varepsilon,R}$. For example, the red colored zone indicates Ω_F. (For interpretation of the references to color in this figure legend, the reader is referred to the web version of this article.)

where

$$M^k(\mathcal{T}) := \left\{ P \in L^2(\Lambda) |\ P_{|T} \in \mathbb{Q}^k(T),\ \forall T \in \mathcal{T} \right\}, \tag{28}$$

and

$$M_0^k(\mathcal{T}) := M^k(\mathcal{T}) \cap \mathbb{C}(\Lambda). \tag{29}$$

Here, $M_0^k(\mathcal{T})$ is the subspace of $M^k(\mathcal{T})$ consisting of the globally continuous piecewise continuous functions ($\mathbb{C}$).

For simplicity, currently, the transport system for proppant is discretized by using EG with constant functions. Thus, the spatial approximation of C is computed using piecewise constants, given in the finite element space $M^0(\mathcal{T})$, which is defined as,

$$M^0(\mathcal{T}) := \{W \in L^2(\Lambda) \mid W|_T \in \mathbb{Q}^0(T), \forall T \in \mathcal{T}\}. \tag{30}$$

3.3. Decomposing the fractured domain with smoothed indicator functions

With the provided spatial discretization, we determine the subdomains $\Omega_F(t)$ and $\Omega_R(t)$ for solving pressure, proppant/saturation and crack width in the fracture and the reservoir. The challenge is that we assumed in Section 2 a sharp fracture interface Γ_F for the modeling, but the phase-field fracture framework yields a diffusive (smeared) interface. To this end, we repartition the time-dependent subdomains $\Omega_R(t)$ and $\Omega_F(t)$ by introducing the diffusive transition (interface) zone (Ω'_ε), and the transition interface zone is again partitioned to a fracture part ($\Omega'_{\varepsilon,F}$) and a porous medium part ($\Omega'_{\varepsilon,R}$). In addition, $\Omega'_R(t)$, and $\Omega'_F(t)$ are introduced, see Fig. 6(b) for the details.

By construction, a natural choice for this indicator function is the phase-field variable Φ, and we start by introducing (smoothed) indicator functions χ_F and χ_R to define Ω'_F and Ω'_R. In particular, we propose

Definition 3.1. The indicator functions χ_F and χ_R are defined by:

$$\chi_F(\cdot,t,\Phi) := \begin{cases} 1, & \text{if } \Phi(\mathbf{x},t) \le x_1 \\ 0, & \text{if } \Phi(\mathbf{x},t) \ge x_2 \\ -\dfrac{(\Phi - x_2)}{(x_2 - x_1)}, & \text{otherwise} \end{cases} \qquad \chi_R(\cdot,t,\Phi) := \begin{cases} 1, & \text{if } \Phi(\mathbf{x},t) \ge x_2 \\ 0, & \text{if } \Phi(\mathbf{x},t) \le x_1 \\ \dfrac{(\Phi - x_1)}{(x_2 - x_1)}, & \text{otherwise} \end{cases} \tag{31}$$

These functions are depicted in Fig. 6(a).

Thus, we define the following subdomains:

- $\Omega'_R(t)$ is where $\chi_R = 1$ and $\chi_F = 0$, and
- $\Omega'_F(t)$ is where $\chi_F = 1$ and $\chi_R = 0$.
- Moreover the transition zone (Ω'_ε) is where $\chi_R \neq 0, 1$ and $\chi_F \neq 0, 1$, but $0 < \chi_R, \chi_F < 1$ and $\chi_R + \chi_F = 1$.

We note that is Ω'_ε divided by $\Omega'_{\varepsilon,F}$ and $\Omega'_{\varepsilon,R}$, by depending on the choice of Γ_F. Here, Γ_F is defined as discussed in Section 2.7 by choosing C_{LS}. Thus, we redefine the subdomains as $\Omega_F := \Omega'_F \cup \Omega'_{\varepsilon,F}$ and $\Omega_R := \Omega'_R \cup \Omega'_{\varepsilon,R}$. Finally, χ_R is multiplied to Eq. (12) and χ_F is multiplied to Eq. (13), and the choices for $x_1 \in (0, 0.5)$ and $x_2 \in (0.5, 1.)$ are studied in detail in [9].

4. Coupling algorithms, parallel solvers, and adaptivity

In this section, we describe the overall coupling algorithm and provide further details on the specific nonlinear and linear solvers, their parallelization as well as local mesh adaptivity. As previously described, an important aspect has been on physics-based carefully-tailored discretization schemes. Obviously each subproblem demands a different type of solver, because each has different physical conservation properties.

4.1. The fixed-stress split iterative method

The first approach to solve the coupled flow and geomechanics system with the phase field is the fully implicit one, in which the flow and mechanics problems are solved simultaneously. This is an unconditionally stable approach, and results in the most accurate solution. However, its main drawback is its huge computational cost, which imposes several computational challenges on the underlying linear solver.

The most successful method in our proposed algorithm is to employ the fixed-stress iterative coupling approach to couple fluid flow with geomechanics for the phase-field fractures. The fixed-stress split iterative method [88–98] has been a standard approach in petroleum engineering for decoupling geomechanics and flow in porous media and this approach has an efficient computational cost, depending on the convergence stopping criterion enforced [91,99–103].

The fixed-stress approach is an iterative coupling, and solves the two problems (fluid and geomechanics) in the sequential fashion. In particular, it consists of imposing constant volumetric mean total stress. This means that the mean stress

$$\sigma_v = \sigma_{v,0} + K_{dr} \nabla \cdot (\mathbf{u} - \mathbf{u}_0) - \alpha (p - p_0), \tag{32}$$

is kept constant at the half-time step. Here, $\sigma_{v,0}$ is the initial stress, $\mathbf{u}_0$ is the initial displacement, and p_0 the initial pressure. The fixed-stress coefficient is $K_{dr} = \frac{3\lambda+2\mu}{3}$. Detailed studies with a given, fixed, fracture are provided in [102]. Fixed-stress methodologies for propagating fractures using phase-field methods were proposed in [39] and extended to a multirate formulation in [41].

The iterative process reads: for $l = 0, 1, 2, \ldots$,

$$\begin{aligned} \left(\frac{1}{M} + \frac{\alpha^2}{K_{dr}}\right) \partial_t p^{l+1} + \nabla \cdot \left(\frac{K}{\eta}(\rho_F \mathbf{g} - \nabla p^{l+1})\right) &= -\frac{\alpha}{K_{dr}} \partial_t \sigma_v^l + f, \\ &= f - \alpha \nabla \cdot \partial_t \mathbf{u}^l + \frac{\alpha^2}{K_{dr}} \partial_t p^l \qquad (33) \\ -\nabla \cdot \sigma^{por}(\mathbf{u}^{l+1}) + \alpha (\nabla p^{l+1}), = 0, & \qquad (34) \end{aligned}$$

until the convergence criteria is met. As stopping condition, we either use simply

$$\max\{\|\mathbf{u}^l - \mathbf{u}^{l-1}\|_{L^2(\Lambda)}, \|p^l - p^{l-1}\|_{L^2(\Lambda)}\} \leq TOL_{FS}$$

or take the residual with respect to the porosity, e.g. [91]. The extension to incorporate the phase-field equation results in Algorithm 1.

4.1.1. Fixed-stress algorithm for fluid-filled fracture systems

As previously noted, we first solve for the pressure, which is in the case of fractures realized as a pressure diffraction problem:

Formulation 4.1. *For each time t^{n+1} we iterate for $l = 0, 1, 2, \ldots$ to find $P^{l+1} \in \mathbb{W}(\mathcal{T})$ such that*

$$[B(P^{n+1})(\omega)]^{l+1} = [B_R(P^{n+1})(\omega)]^{l+1} + [B_F(P^{n+1})(\omega)]^{l+1} = 0 \quad \forall \omega \in \mathbb{W}(\mathcal{T}),$$

Algorithm 1 Fixed-stress for phase field fluid-filled fractures in porous media

```
At each time $t^n$
repeat
    Solve two-field fixed-stress (inner loop).
      Solve the (linear) pressure diffraction, Formulation 4.1.
      Solve the (nonlinear) fully-coupled elasticity phase field, Formulation 4.3.
until Stopping criterion
        $\max\{\|p^l - p^{l-1}\|, \|\mathbf{u}^l - \mathbf{u}^{l-1}\|, \|\varphi^l - \varphi^{l-1}\|\} \le \mathrm{TOL}_{\mathrm{FS}}, \quad \mathrm{TOL}_{\mathrm{FS}} > 0,$
    for fixed-stress split is satisfied.
Set: $(p^n, \mathbf{u}^n, \varphi^n) := (p^l, \mathbf{u}^l, \varphi^l)$.
Increment $t^n \to t^{n+1}$.
```

where

$$\begin{aligned}
[B_R(P^{n+1})(\omega)]^{l+1} := \chi_R(\Phi^{l+1})\Big(&\int_\Lambda \rho_R^0\Big(\frac{1}{M}+\frac{3\alpha^2}{3\lambda+2\mu}\Big)\Big(\frac{P^{l+1}-P^n}{\Delta t}\Big)\cdot\omega\, d\mathbf{x}\\
&+\int_\Lambda \frac{K_R\rho_R^0}{\eta_R}(\nabla P^{l+1}-\rho_R^0\mathbf{g})\nabla\omega\, d\mathbf{x}+\int_\Lambda \alpha\nabla\cdot\Big(\frac{\mathbf{U}^l-\mathbf{U}^n}{\Delta t}\Big)\cdot\omega\, d\mathbf{x}\\
&-\int_\Lambda\Big(\frac{3\alpha^2}{3\lambda+2\mu}\Big)\Big(\frac{P^l-P^n}{\Delta t}\Big)\omega\, d\mathbf{x}-\int_\Lambda q_R\omega\, d\mathbf{x}\Big),\quad \forall\omega\in\mathbb{W}(\mathcal{T}),
\end{aligned}\tag{35}$$

$$\begin{aligned}
[B_F(P^{n+1})(\omega)]^{l+1} := \chi_F(\Phi^{l+1})\Big(&\int_\Lambda \rho_F^0 c_F\Big(\frac{P^{l+1}-P^n}{\Delta t}\Big)\omega\, d\mathbf{x}\\
&+\int_\Lambda \frac{K_F\rho_F^0}{\eta_F}(\nabla P^{l+1}-\rho_F^0\mathbf{g})\nabla\omega\, d\mathbf{x}-\int_\Lambda (q_F-q_L)\omega\, d\mathbf{x}\Big),\quad \forall\omega\in\mathbb{W}(\mathcal{T}).
\end{aligned}\tag{36}$$

Remark 4.2. Even though we have formulated two equations, one can observe that both are of a generalized parabolic type [59,60]. To this end, only one equation must be implemented as stated in Formulation 2.5.

Then, we solve for the displacement-phase field inequality:

Formulation 4.3. *We solve for the displacements* $\mathbf{U}^{l+1}\in\mathbb{V}_0(\mathcal{T})$ *and the phase field* $\Phi^{l+1}\in\mathbb{Z}(\mathcal{T})$ *such that:*

$$A(\mathbf{U}^{l+1},\Phi^{l+1})(\mathbf{w},\psi-\Phi^{l+1})\ge 0\quad \forall\{\mathbf{w},\psi\}\in\mathbb{V}_0(\mathcal{T})\times\mathbb{Z}(\mathcal{T}),\tag{37}$$

where

$$\begin{aligned}
A(\mathbf{U}^{l+1},\Phi^{l+1})(\mathbf{w},\psi-\Phi^{l+1}) &= \int_\Lambda g_D(\Phi^{l+1})\sigma^+(\mathbf{U}^{l+1}):e(\mathbf{w})\, d\mathbf{x}+\int_\Lambda \sigma^-(\mathbf{U}^{l+1}):e(\mathbf{w})\, d\mathbf{x}\\
&-\int_\Lambda(\alpha-1)g_D(\Phi^{l+1})P^{l+1}\nabla\cdot\mathbf{w}\, d\mathbf{x}+\int_\Lambda g_D(\Phi^{l+1})\nabla P^{l+1}\cdot\mathbf{w}\, d\mathbf{x}\\
&+(1-\kappa)\int_\Lambda \Phi^{l+1}\sigma^+(\mathbf{U}^{l+1}):e(\mathbf{U}^{l+1})(\psi-\Phi^{l+1})\, d\mathbf{x}\\
&-2(\alpha-1)\int_\Lambda \Phi^{l+1}P^{l+1}\nabla\cdot\mathbf{U}^{l+1}(\psi-\Phi^{l+1})\, d\mathbf{x}+\int_\Lambda 2\Phi^{l+1}\nabla P^{l+1}\cdot\mathbf{U}^{l+1}(\psi-\Phi^{l+1})\, d\mathbf{x}\\
&-G_c\int_\Lambda \frac{1}{\varepsilon}(1-\Phi^{l+1})(\psi-\Phi^{l+1})\, d\mathbf{x}\\
&+G_c\int_\Lambda \varepsilon\nabla\Phi^{l+1}\cdot\nabla(\psi-\Phi^{l+1})\, d\mathbf{x}\ge 0,\quad \forall\{\mathbf{w},\psi\}\in\mathbb{V}_0(\mathcal{T})\times\mathbb{Z}(\mathcal{T}).
\end{aligned}\tag{38}$$

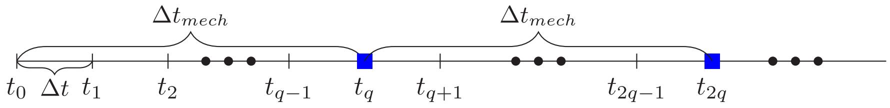

Fig. 7. Illustrating the time grids for the multirate algorithm. The time step for mechanics, $\Delta t_{mech} = q\Delta t$, is q times larger than the time step for flow Δt. The fixed-stress iteration (Section 4.1.1) is performed every Δt_{mech} in the (blue) squares.

Remark 4.4 (*Stopping Criterion*)**.** The iteration between Formulations 4.1 and 4.3 is completed if

$$\max\{\|\mathbf{U}^{l+1} - \mathbf{U}^l\|_{L^2(\Lambda)}, \|P^{l+1} - P^l\|_{L^2(\Lambda)}, \|\Phi^{l+1} - \Phi^l\|_{L^2(\Lambda)}\} < TOL_{FS}.$$

Then we set

$$P^{n+1} := P^{l+1}, \ \ \Phi^{n+1} := \Phi^{l+1}, \ \ \mathbf{U}^{n+1} := \mathbf{U}^{l+1}.$$

Remark 4.5. For pressurized fractures, no fixed-stress splitting is necessary, since the pressure (flow) is a given right-hand-side quantity (e.g. $\alpha = 0$ and $p = const$) and only for fluid filled fractures (e.g. $\alpha = 1$), the fixed-stress iteration has to be employed.

4.1.2. Multirate phase-field time splitting

We further extend the phase-field fixed-stress algorithm to a multirate phase-field scheme in time. We assume that the geomechanics part (namely phase-field plus displacements) can work with coarser time step sizes than the pressure diffraction problem. Consequently, we perform several flow time steps within one phase-field-displacement step; see Fig. 7. Extensive work was undertaken in [104,105]. We also mention [106]. Previous results for a phase-field fracture system were published in [41]. Therein, we found that the current coupling between multirate fixed-stress and phase-field must be further improved when the fracture is propagating. The reason being that a propagating fracture has rapid changes in the pressure and the displacements.

We introduce two time grids: one for the pressure diffraction system (4.1) with the time step size $\Delta t := t_n - t_{n-1}$, and one for the displacement phase-field system (4.3) with the time step size $\Delta t_{mech} := t^{mech}_{nq} - t^{mech}_{q}$. Our assumption is that the pressure problem requires a finer time grid than the geomechanics/fracture problem, i.e., $\Delta t_{mech} > \Delta t$. We assume uniform time grids.

Then one cycle of the multirate phase-field problem reads:

Algorithm 4.6 (*Multirate Phase-field Fixed-stress — One Step*)**.** At time point t_n:

1. Take Formulation 4.1. For $m = 1, \dots, q$: Find $P^{n+m} \in \mathbb{W}(\mathcal{T})$ such that
$$[B(P^{n+m})(\omega)] = 0 \quad \forall \omega \in \mathbb{W}(\mathcal{T}).$$
2. Take Formulation 4.3 and compute once the displacement phase-field problem at $t_q = t_{mech} = t_{mech} + \Delta t_{mech} = t_{mech} + q\Delta t$. Find $(\mathbf{U}^{n+q}, \Phi^{n+q}) \in \mathbb{V}_0(\mathcal{T}) \times \mathbb{Z}(\mathcal{T})$ such that
$$A(\mathbf{U}^{n+q}, \Phi^{n+q})(\mathbf{w}, \psi - \Phi^{n+q}) \geq 0 \quad \forall \{\mathbf{w}, \psi\} \in \mathbb{V}_0(\mathcal{T}) \times \mathbb{Z}(\mathcal{T})$$
3. At t_{n+q} call the fixed-stress Algorithm 1 and iterate for $l = 0, 1, 2, \dots$ until convergence. Denote the index in the converged state with l^*.
4. Set $P^{n+q} := (P^{n+q})^{l^*}, \mathbf{U}^{n+q} := (\mathbf{U}^{n+q})^{l^*}, \Phi^{n+q} := (\Phi^{n+q})^{l^*}$.
5. Go to Step 1.

Remark 4.7. Obviously, the choice q depends on the specific problem under consideration. Moreover, the algorithm may be switched in case we need smaller time steps for the mechanics problem and coarser time steps for the flow part.

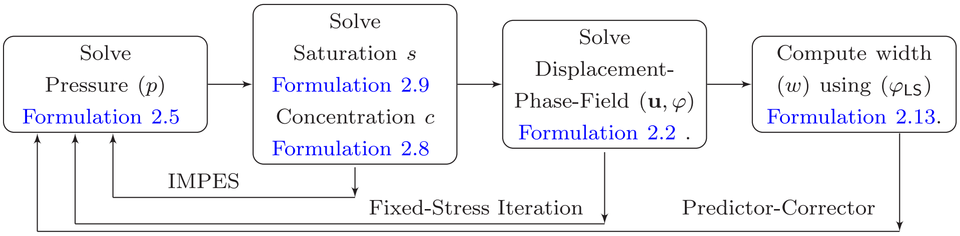

Fig. 8. The global algorithm flowchart.

4.2. Global coupling algorithm (as of the year 2019)

Fig. 8 illustrates the global solution algorithm for our proposed coupled system. After solving the phase-field and the displacement monolithically, the pressure equation is coupled by the fixed-stress iteration. For two phase flow, the saturation equation and the pressure equation are coupled by iterative Implicit Pressure Explicit Saturation formulation (IMPES), which is embedded in the fixed-stress iteration. The predictor–corrector adaptive mesh refinement method iterates each time step to ensure the stability of the scheme.

Each component can be seen as a module and easily modified or replaced. For instance if a single phase-fluid in a fractured porous medium shall be solved, the saturation/concentration module can be simply removed.

4.3. Nonlinear and linear solvers

We briefly discuss the numerical solvers to treat the discretized formulations for displacements, phase-field, pressure, proppant/saturation, and crack width. The overall problem is a large coupled framework, which is modeled for two- and three dimensional settings. Specifically, for the later one, local mesh adaptivity and parallel computing are indispensable ingredients in order to obtain reasonable wall clock times.

4.3.1. Quasi-monolithic solution of displacements/phase-field

The nonlinear quasi-monolithic displacement/phase-field system is solved with Newton's method and line search algorithms. We recall that we have three types of nonlinearities:

1. the nonlinear couplings $g(\Phi)\sigma^+(\mathbf{U})$ and $\Phi\sigma^+(\mathbf{U}) : e(\mathbf{U})$
2. stress-splitting into $\sigma^+(\mathbf{U})$ and $\sigma^-(\mathbf{U})$
3. the crack irreversibility constraint; requiring to work with convex sets rather than linear function spaces.

The first problem is resolved by using a linear-in-time extrapolation $g(\tilde{\Phi})\sigma(\mathbf{U})$; for details see [7] and also Section 4.3.4. The second problem is simply kept and treated with a nonlinear Newton solver as our solution algorithm. The third problem is resolved by implementing a primal–dual-active set strategy. The latter one can be interpreted as a semi-smooth Newton method [107]. Consequently, the second and third problems can be combined into one single Newton loop as outlined in Algorithm 4.8.

Algorithm 4.8 (*Phase-field Semi-smooth Newton*). Set $(\mathbf{U}^0, \Phi^0) := (\mathbf{U}^n, \Phi^n)$ be the initial Newton guess. Iterate for $k = 0, 1, 2, \ldots$:

1. Assemble residual $A(\mathbf{U}^k, \Phi^k)(\cdot, \cdot)$
2. Compute active set $\mathcal{A}_k = \{i \mid (B^{-1})_{ii}(A(\cdot, \cdot)(\cdot, \cdot)_k)_i + c((\delta\mathbf{U}^k, \delta\Phi^k))_i > \varepsilon\}$
3. Assemble matrix $G = \nabla^2 E_\varepsilon(\mathbf{U}^k, \Phi^k)$ and right-hand side $F = -\nabla E_\varepsilon(\mathbf{U}^k, \Phi^k)$
4. Eliminate rows and columns in $\mathcal{A}_k$ from G and F to obtain $\widetilde{G}$ and $\widetilde{F}$. The corresponding residual is denoted by $\widetilde{A}(\mathbf{U}_h^k, \Phi^k)(\cdot, \cdot)$.
5. Solve linear system with a block-preconditioned GMRES scheme: $\widetilde{G}(\delta\mathbf{U}^k, \delta\Phi^k)^T = \widetilde{F}$, i.e, find $(\delta\mathbf{U}^k, \delta\Phi^k) \in \mathbb{V}_0(\mathcal{T}) \times \mathbb{Z}(\mathcal{T})$ with
$$\nabla^2 E_\varepsilon(\mathbf{U}^k, \Phi^k)((\delta\mathbf{U}^k, \delta\Phi^k), (\mathbf{w}, \psi)) = -\nabla E_\varepsilon(\mathbf{U}^k, \Phi^k)(\mathbf{w}, \psi) \tag{39}$$
for all $(\mathbf{w}, \psi) \in \mathbb{V}_0(\mathcal{T}) \times \mathbb{Z}(\mathcal{T})$. Here, $\nabla^2 E_\varepsilon = A'(\mathbf{U}, \Phi)((\delta\mathbf{U}, \delta\Phi), (\cdot, \cdot))$ and $\nabla E_\varepsilon = A(\mathbf{U}, \Phi)(\cdot, \cdot)$.

6. Find a step size $0 < \omega \leq 1$ using line search to get

$$(\mathbf{U}^{k+1}, \Phi^{k+1})^T = (\mathbf{U}^k, \Phi^k)^T + \omega(\delta \mathbf{U}^k, \delta \Phi^k)^T,$$

   with $\|\widetilde{A}(\mathbf{U}_h^{k+1}, \Phi^{k+1})(\cdot, \cdot)\| < \|\widetilde{A}(\mathbf{U}^k, \Phi^k)(\cdot, \cdot)\|$.

7. Check the stopping criteria:
   - the active set $\mathcal{A}_k$ does not change
   - and it holds $\|\widetilde{A}(\mathbf{U}^k, \Phi^k)(\cdot, \cdot)\| < \mathrm{TOL}$

   If both criteria are fulfilled: algorithm converged.
   If not, $k \mapsto k+1$ and go to Step 1.

4.3.2. GMRES iterative linear solution and multigrid preconditioning

The linear systems (39) arising at each Newton step read formally:

$$\begin{pmatrix} M_{uu} & 0 \\ M_{\varphi u} & M_{\varphi\varphi} \end{pmatrix} \begin{pmatrix} \delta \mathbf{U} \\ \delta \Phi \end{pmatrix} = \begin{pmatrix} F_u \\ F_\varphi \end{pmatrix}. \tag{40}$$

The block $M_{u\varphi}$ is zero because we use in the displacement equation the extrapolation $\tilde{\Phi}$. Consequently, for the directional derivative in Φ, we have

$$\frac{d}{d\Phi} g(\tilde{\Phi})\sigma^+(\mathbf{U}) = 0;$$

see [7] for more details. The resulting time-lagging error by using $\tilde{\Phi}$ rather than Φ can be reduced as explained in Section 4.3.4. The performance of fully monolithic solvers was evaluated [24,25]. Therein, $M_{u\varphi} \neq 0$.

Observing carefully the diagonal entries, we see that these are of elliptic type weighted by $g(\Phi)$ and $1/\varepsilon$. Of course, a direct solver is not relevant due to the applications we are considering. A robust and efficient approach are iterative solvers (for instance GMRES) with a multigrid preconditioner.

Due to the triangular structure of the matrix in (40), a good preconditioner is:

$$P_{cond}^{-1} = \begin{pmatrix} \tilde{M}_{uu}^{-1} & 0 \\ 0 & \tilde{M}_{\varphi\varphi}^{-1} \end{pmatrix}$$

Since the entries $\tilde{M}_{uu}$ and $\tilde{M}_{\varphi\varphi}$ are elliptic, a good choice is either a geometric or algebraic multigrid method to compute the inverse matrices. We assume the existence of spectrally equivalent approximations $\tilde{M}_{uu}^{-1}$ and $\tilde{M}_{\varphi\varphi}^{-1}$, which correspond to linear elasticity and a mixture of a reaction–diffusion equation, respectively. The eigenvalues are given by the generalized eigenvalues of the systems $\tilde{M}_{kk} = \lambda_E M_{kk}$ $(k = u, \varphi)$. For convenience of our underlying code basis, we employ a single V-cycle of algebraic multigrid from Trilinos [108].

4.3.3. Performance studies of Newton's method and the linear gmres solver

The performance of the solvers as a stand-alone block was recently evaluated in [10] indicating that the parallel code is scalable from 16 to 2048 processors with 43 to 52 GMRES iterations per Newton step for the 2d Sneddon benchmark [109]. The Newton converges within 2 or 3 steps. However the active set method (in order to realize the crack irreversibility constraint) needs about 4 to 8 iterations. Therefore, our combined Newton solver needs between 4 and 10 iterations per time step. We also refer to Chapter 14 in [110] for recent parallel performance tests of the two-dimensional Sneddon test.

4.3.4. An iteration on the phase-field extrapolation

An improvement of accuracy can be achieved when a few subiterations on the extrapolation $\tilde{\Phi}$ are executed. The approach reads:

Algorithm 4.9 (*Iterating on the Extrapolation*)**.** We assume to be in time step t_n.

1. Let Φ^{n-2} and Φ^{n-1} be the given two previous time step solutions;
2. Set $\Phi^{n,-2} := \Phi^{n-2}$ and $\Phi^{n,-1} := \Phi^{n-1}$

3. Construct the linear extrapolation:

$$\tilde{\Phi}^{n,0} = \Phi^{n,-2}\frac{t_n - t_{n-1}}{t_{n-2} - t_{n-1}} + \Phi^{n,-1}\frac{t_n - t_{n-2}}{t_{n-1} - t_{n-2}}$$

4. Set $\mathbf{U}^{n,0} := \mathbf{U}^{n-1}$ and $\Phi^{n,0} := \Phi^{n-1}$;
5. For $i = 1, \dots, N_{IE}$:
   (a) Find $(\mathbf{U}^{n,i}, \Phi^{n,i})$ by solving the displacement phase-field system with $\mathbf{U}^{n,i-1}$, $\Phi^{n,i-1}$, $\tilde{\Phi}^{n,i-1}$.
   (b) Construct a new extrapolation:

$$\tilde{\Phi}^{n,i} = \Phi^{n,i-2}\frac{t_n - t_{n-1}}{t_{n-2} - t_{n-1}} + \Phi^{n,i-1}\frac{t_n - t_{n-2}}{t_{n-1} - t_{n-2}}.$$

   (c) Increment $i \to i + 1$.
6. Set $\mathbf{U}^n := \mathbf{U}^{n,N_{IE}}$ and $\Phi^n := \Phi^{n,N_{IE}}$.

Remark 4.10. Some results on the performance of the iteration on the extrapolation in pure mechanics test cases can be found in [110][Chapter 9].

4.3.5. Pressure, proppant, saturation, crack width problem

These subproblems are modeled as diffraction problems using EG methods as previously described and solved with the generalized minimal residual method (GMRES) solvers with diagonal block-preconditioning. Finally, the linear-elliptic crack width problems are solved with a parallel conjugate gradient (CG) solver and symmetric successive over-relaxation (SSOR) preconditioning.

4.4. Local mesh adaptivity using a predictor–corrector strategy

Mathematically as well as by mechanical requirements the phase-field model parameter might be a small value. This yields in a heavy computational burden if $\varepsilon \ll 1$ because we must basically ensure that

$$\varepsilon > h$$

when working with bilinear finite elements. Simultaneously we do not want to change ε during a simulation since this would mean that we change the (phase-field) model.

Our strategy at hand is a predictor–corrector technique proposed in [7] and extended to three-dimensions in [6]. Here, we choose $\varepsilon > h$ at the beginning of the computation. Our aim is to work with reasonable coarse meshes outside the fracture region. In those parts of the domain $\varepsilon > h$ may be violated. To this end, we arrive at a four-step procedure (see also Fig. 9):

Algorithm 4.11 (*Predictor–corrector Mesh Adaptivity*)**.** At t_n:

1. Given the current solution $\{\mathbf{U}, \Phi\}$ at t_n;
2. Solve for $\{\tilde{\mathbf{U}}, \tilde{\Phi}\}$ and predict the fracture path at t_{n+1};
3. Refine the mesh regarding to $\{\tilde{\mathbf{U}}, \tilde{\Phi}\}$ and go afterward back to the solution $\{\mathbf{U}, \Phi\}$;
4. Solve for on the new mesh for $\{\mathbf{U}_{n+1}, \Phi_{n+1}\}$ at t_{n+1}.

It has been shown in [7] (two dimensional) and [6,9] (three dimensional) that this procedure is efficient and robust. As refinement criterion we take simply a threshold value of the phase-field variable, i.e., once $\Phi < C_A$ with $0 < C_A < 1$, e.g., $C_A \sim 0.6$, we flag a mesh element for refinement.

5. Representative numerical examples

In this final section, first we summarize the development of the code and present several representative numerical experiments to emphasize the capability of our proposed algorithm and the simulator. This summary also includes brief statements of former code versions.

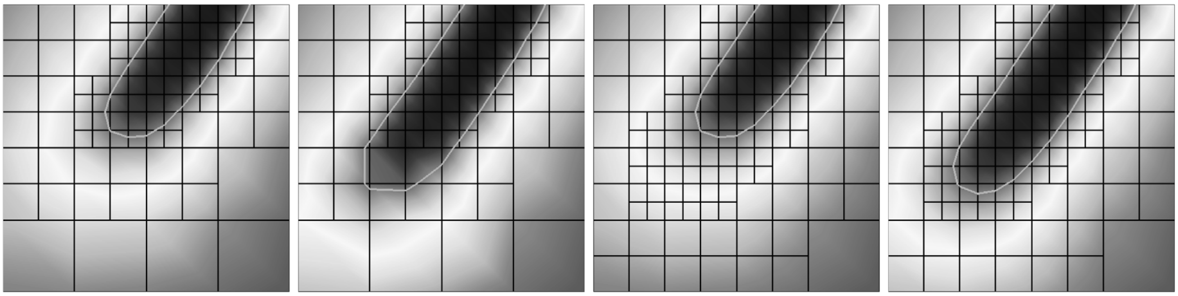

(a) (b) (c) (d)

Fig. 9. Mode of operation of predictor–corrector mesh adaptivity: (a) old state at t_n. (b) advance in time, crack leaves fine mesh. (c) refine and go back in time (interpolate old solution). (d) advance in time t_{n+1} on new mesh. Repeat until mesh does not change anymore. As refinement indicator, we choose for instance $C_A = 0.6$ (white contour line around black fracture zone).

5.1. Integrated Phase Field Advanced Crack Propagation Simulator (IPACS)

Along with the mathematical modeling and the design of numerical algorithms, we have been continuously developing software. These developments have been resulted in a robust and efficient framework called IPACS: Integrated Parallel Advanced Crack Propagation Simulator.

The initial IPACS code was established in [6,7,9] and enhancements to different applications were added. Recent versions are in-house codes, but all algorithms have been published and the corresponding frameworks can be re-implemented.

IPACS is based on the C++ finite element library deal.II [111–113] with MPI (message passing interfaces) and p4est [114] packages for the octree mesh adaptivity. For the linear solver, specifically algebraic multigrid preconditioning, Trilinos [108] is employed.

5.1.1. Version 1.0 and version 2.0: pressurized fracture in two and three dimensions

In the basic version [7], the phase-field fracture framework employed two variables, namely the displacements and the phase-field variable. Version 1.0 includes two different algorithms: a decoupled approach and a monolithic technique. For the monolithic solver, a primal–dual active set method for the crack irreversibility was developed. The resulting problem is treated in a quasi-monolithic fashion in which the phase-field variable is time-lagged through an extrapolation-in-time. In addition, predictor–corrector mesh adaptivity was implemented and the efficiency was fully studied. Furthermore, the code can treat pressurized fractures, where the pressure is not yet a solution variable, but a given, fixed, quantity. The code was developed for two-dimensional problems.

Later, Version 2.0 code was extended to three dimensional cases with parallel computing using MPI [6]. In previous versions, several different algorithms were tested for irreversibility condition such as simple penalization, augmented Lagrangian, and active-set method, but for the three dimensional case, the primal–dual active-set method appears optimal.

5.1.2. Version 3.0: fluid-filled fracture propagation for two and three dimensions

The major increment of this version was to couple the system with a fluid pressure diffraction equation [12]. Two different solvers were developed. One based on a monolithic scheme [17] and the other on fixed-stress splitting [39].

5.1.3. Version 4.0: enriched Galerkin (EG) for flow and proppant transport

In this version, the physics were enhanced to model proppant transport in the fracture flow. Thus, a transport equation described in a previous section was implemented and coupled. To provide locally conservative numerical discretization, an enriched Galerkin (EG) finite element method for the pressure equation was utilized [33].

5.1.4. Version 5.0: two-phase flow in the fracture using an IMPES scheme

In the current version, a two-phase fracture flow model established in [34] was implemented. Here, an additional saturation equation is employed to distinguish between the different phases and to compute relative permeabilities. An IMPES iterative coupling scheme is employed for saturation and pressure system.

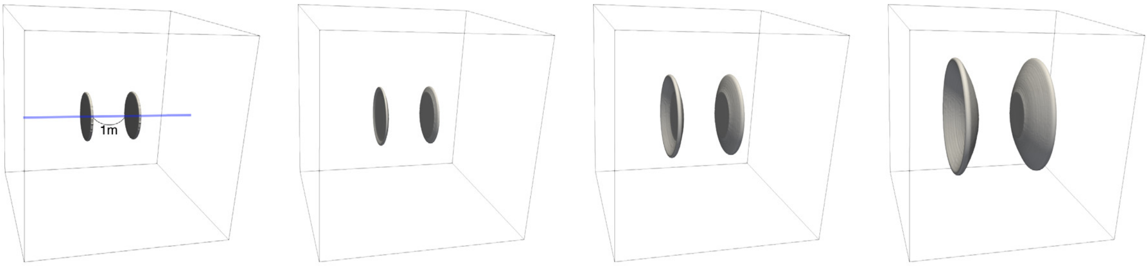

(a) $n = 0$ (b) $n = 65$ (c) $n = 70$ (d) $n = 75$

Fig. 10. Initial setup: (a) Two initial parallel fractures are placed where the distance between these fractures is $1m$. (b)–(d) Propagation of two parallel fractures for increasing pressure for each time step n. We observe the stress shadowing effect that causes the two fractures to curve away.

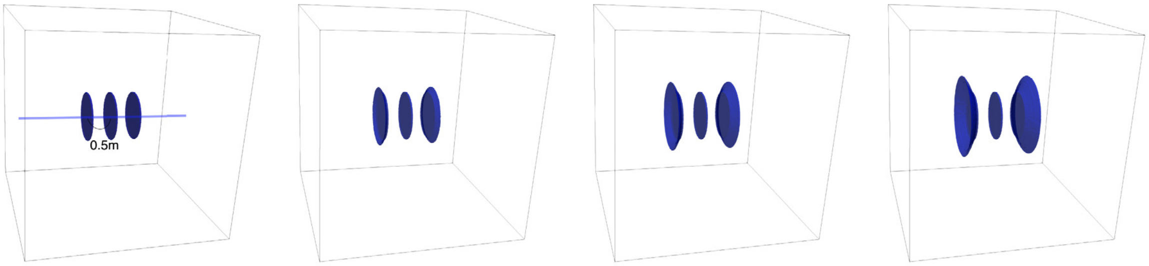

(a) $n = 0$ (b) $n = 68$ (c) $n = 70$ (d) $n = 72$

Fig. 11. (a) Three initial parallel fractures, where the distance between each fractures is $0.5m$. (b)–(d) Propagation of two parallel fractures for increasing pressure for each time step n.

5.2. *Test scenario 1: fracture propagation with a given pressure*

In this section, we present pressurized fracture propagation examples, where $\alpha = 0$ [9]. The pressure is given as a constant, but linearly increasing in time for the fracture propagation. The computations utilize IPACS-versions 1 and 2.

5.2.1. *Two and three parallel fractures*

We present the fracture propagation for multiple interacting parallel fractures, which are referred to a stress shadowing effect; see [6,15,115].

In the domain $\Lambda = (0, 4\,\text{m})^3$, first we set two initial penny shape fractures as shown in Fig. 10(a). The left fracture is centered at $(1.5\,\text{m}, 2\,\text{m}, 2\,\text{m})$ with radius $r = 0.5\,\text{m}$ on $x = 1.5\,\text{m}$ and the right fracture is centered at $(2.5\,\text{m}, 2\,\text{m}, 2\,\text{m})$ with radius $r = 0.5\,\text{m}$ on $x = 2.5\,\text{m}$. Both fractures have thickness of $2h_{\text{min}}$. Here, $G_c = 1.0\,\text{Pa}\,\text{m}$ and Lamé coefficients are given as $G = 4.2 \times 10^7$ Pa and $\lambda = 2.8 \times 10^7$ Pa. The fractures grow by a given constant pressure in space and linearly increasing in time; $p = t \times 5 \times 10^4$ Pa, where t is the current time. The discretization parameters are $\Delta t = 0.005$ and $h_{\text{min}} = 0.027\,\text{m}$.

As we observe in Fig. 10, if the distance between the fractures is sufficiently close, then they influence each other via their stress fields, often referred as the stress shadowing effect. The leading corners of the fractures start to grow by curving out from the initial cracks. The interaction between the fractures increases when the fractures become larger and closer. Next, as shown in Fig. 11(a), we increase the number of fractures from two to three, but all other mechanical and numerical constants are kept constant as in the previous example. Fig. 11 shows the propagation of the fractures for each time step. Due to the stress-shadowing effect, the middle fracture does not grow as the pressure is increased.

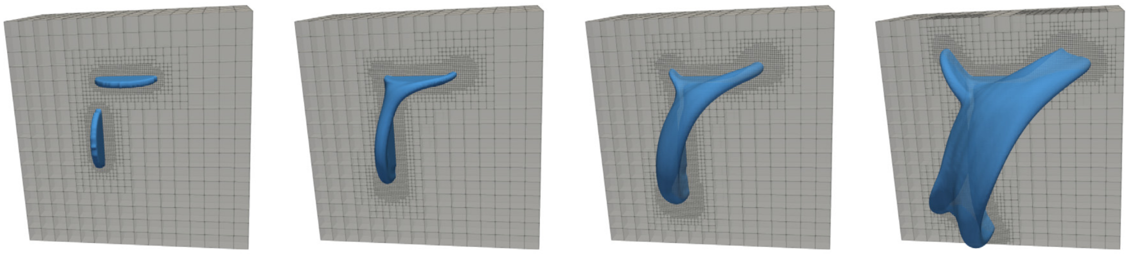

(a) $n = 1$ (b) $n = 16$ (c) $n = 18$ (d) $n = 22$

Fig. 12. Multiple fracture propagation in a three dimensional homogeneous media. Two fractures first join and later branch. Employing the predictor–corrector mesh adaptivity technique, the locally refined mesh follows the crack patterns. This strategy allows for high resolution of ε around the crack pattern but keeps the overall computational cost reasonable since the number of degrees of freedom grows with the cracks.

(a) Initial fractures ($n = 0$) (b) Joining ($n = 15$) (c) Branching ($n = 18$)

Fig. 13. Detailed snapshots of the areas with two cracks at $n = 0$ (a), where the cracks are (b) joining of two fractures at $n = 15$ and (c) starts branching after joining at $n = 18$.

5.2.2. Fractures in homogeneous and heterogeneous media with locally refined meshes

One of the main advantages of the phase-field approach is that the joining and branching of the non-planar fractures are easily determined by the energy functional that we described in the previous sections. Here, we propagate two initial fractures in arbitrary positions with a given increasing pressure and illustrate the propagating non-planar fractures in the three dimensional homogeneous and heterogeneous domains with the locally refined meshes.

In the computational domain $\varLambda = (0, 4\,\mathrm{m})^3$, the top penny shape fracture is centered at $(2\,\mathrm{m}, 3\,\mathrm{m}, 2\,\mathrm{m})$ with radius $r = 0.5\,\mathrm{m}$ in $y = 3\,\mathrm{m}$ and the bottom fracture is centered at $(2.5\,\mathrm{m}, 2\,\mathrm{m}, 2\,\mathrm{m})$ with radius $r = 0.5\,\mathrm{m}$ in $x = 2.5\,\mathrm{m}$. The mechanical parameters are $\nu = 0.2$ and $E = 10^4\,\mathrm{Pa}$ for the homogeneous domain but $E \in [1\,\mathrm{GPa}, 10\,\mathrm{GPa}]$ for the heterogeneous domain [6]. Here the pressure is given by $p = t \times 10^3\,\mathrm{Pa}$ and $p = t \times 1\,\mathrm{MPa}$, for homogeneous and heterogeneous domain, respectively. The discretization parameters are $\varDelta t = 0.01$ and $h_{\min} = 0.054\,\mathrm{m}$.

Fig. 12 shows each time step n of non planar fractures propagating with joining and branching in a homogeneous medium with locally refined meshes near the fractures. In addition, we take detailed snapshots for joining and branching of fractures; see Figs. 13(a)–13(c). These are automatically captured by the proposed phase-field model.

Next, Fig. 14 shows each time step n of non planar fractures propagating with joining and branching in the heterogeneous media.

5.3. Test scenario 2: single-phase flow in the fracture

From this section on, we address fluid filled fracture propagation, where $\alpha = 1$ [9]. The pressure is now computed by the pressure diffraction problem, and is fully coupled with the displacement-phase field system. The selected numerical results below are computed with IPACS-version 3.

5.3.1. Fluid filled penny shape fracture

A single penny shape fracture is initially centered at the middle of the two and three dimensional domain. The mechanical parameters are $\nu = 0.2$ and $E = 10^8\,\mathrm{Pa}$, and the fluid is injected at the center of the fracture with

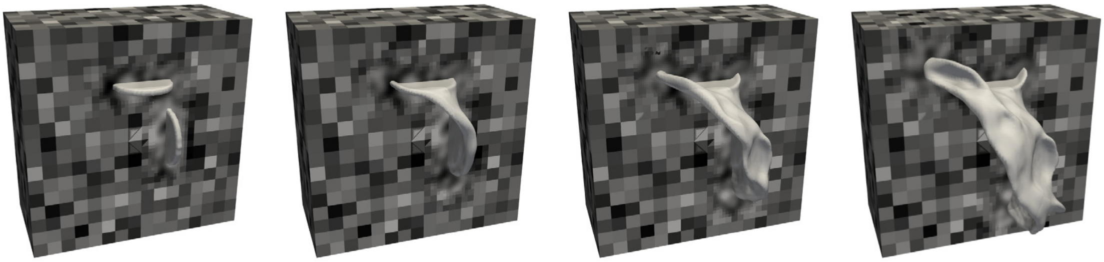
(a) $n = 0$ (b) $n = 32$ (c) $n = 35$ (d) n = 38

Fig. 14. (a) Random heterogeneity by Young's modulus E value range of the shale rock region; $E \in [1\,\text{GPa}, 10\,\text{GPa}]$. (b)–(d) Sequence of snapshots of fractures propagating at each time step number n in a three dimensional heterogeneous media. In these examples, we observe the joining and branching during the non-planar fracture propagation.

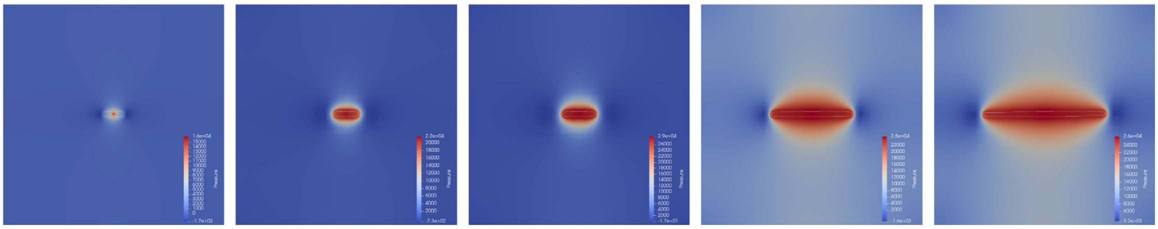
(a) $n = 1$ (b) $n = 10$ (c) $n = 25$ (d) $n = 50$ (e) $n = 80$

Fig. 15. Propagation of a single fluid filled fracture. The contour of the phase field value and the pressure values ($\varphi = 0.5$) at each time step n is illustrated.

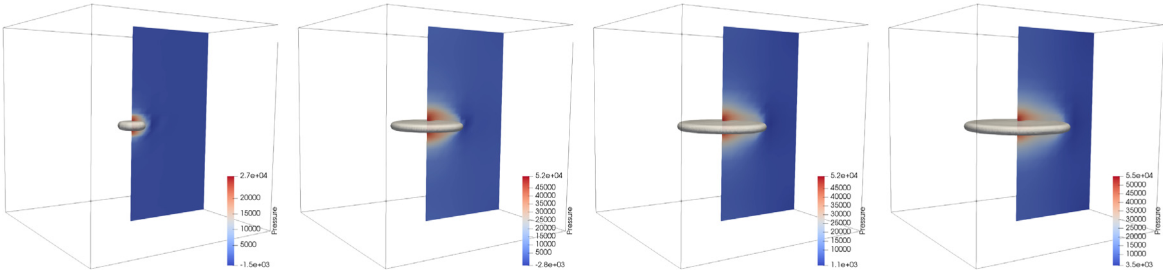

(a) $n = 1$ (b) $n = 30$ (c) $n = 50$ (d) $n = 80$

Fig. 16. Sequence of snapshots of fractures (iso-surface where $\varphi = 0.5$) propagating at each time step n in the three dimensional homogeneous media. The back ground indicates the pressure values.

the constant volume rate of $q_F = 200$ for point source injection. The fluid parameters are given as $\mu_F = \mu_R = 1 \times 10^{-3}\,\text{Ns/m}^2$ and $\rho_R = \rho_F = 1000\,\text{kg/m}^3$. Also other parameters are given as $K_R = 1 \times 10^{-12}$, $\mathbf{g} = 0$, $c_F = 1 \times 10^{-8}$, and the Biot modulus is $M = 2.5 \times 10^8$. Here $h_{\min} = 0.022\,\text{m}$ and the time step is $\Delta t = 0.01$.

Fig. 15 illustrates the propagation of the fracture in the two dimensional domain $\Lambda = (0, 4\,\text{m})^2$ with the initial fracture length $l = 0.25\,\text{m}$. The contour of the phase field value and the pressure values at each time step is illustrated. The pressure increases until the fracture starts propagating and then drops as observed in previous studies.

In the three dimensional domain $\Lambda = (0, 4\,\text{m})^3$, the initial penny shape fracture is centered at $(2\,\text{m}, 2\,\text{m}, 2\,\text{m})$ on $y = 2\,\text{m}$ with the radius $r = 0.25\,\text{m}$. The fluid is injected at the center of the fracture and all the parameters are the same as in the previous two dimensional example. Here $h_{\min} = 0.05\,\text{m}$ and the time step is $\Delta t = 0.01$. The propagation of the fracture is illustrated in Fig. 16 for each time step. The penny shape iso-surface indicates the phase field fracture propagation ($\varphi = 0.5$) with the corresponding pressure values.

(a) $n = 1$ (b) $n = 20$ (c) $n = 40$ (d) $n = 60$

Fig. 17. Sequence of snapshots of fluid filled fractures propagating (phase-field values) for each time step number n.

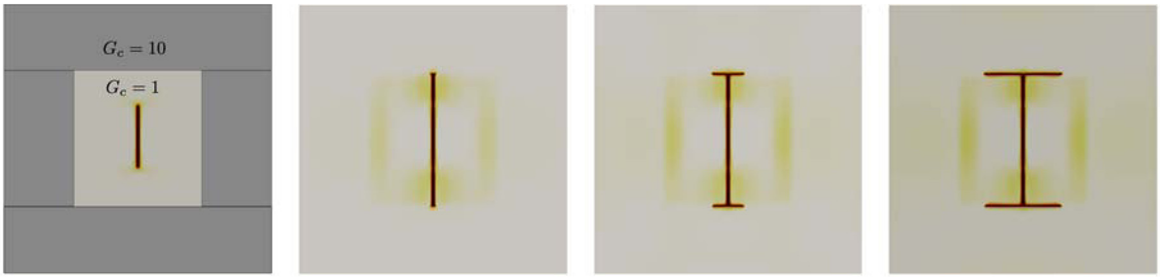

(a) $n = 1$ (b) $n = 40$ (c) $n = 100$ (d) $n = 180$

Fig. 18. Fracture propagating in surrounded layered media. The fracture is positioned at the soft layer and it propagates toward the rigid layer (darker region). We observe the kinked crack near the interface as we see from the experiment [117].

5.3.2. *Multiple fluid filled fractures growing from a wellbore*

In this example, we prescribe the injection/production source on the hole boundary in the middle of the domain as shown in Fig. 17(a). The computational domain is $\Lambda = (-2\,\mathrm{m}, 2\,\mathrm{m})^2 \backslash \mathbb{O}$, where $\mathbb{O} := \{\mathbf{x} \mid |\mathbf{x} - \mathbf{c}| \leq r\}$ is the circle with the center $\mathbf{c} = (0\,\mathrm{m}, 0\,\mathrm{m})$ and the radius $r = 0.1\,\mathrm{m}$, which represents the wellbore. The initial fractures are positioned at $(0 - h_{\min}, 0 + h_{\min}) \times (0.1, 0.5)$ and $(0.1, 0.5) \times (0 - h_{\min}, 0 + h_{\min})$, thus the length is $0.4\,\mathrm{m}$; see Fig. 17(a). The mechanical parameters are $\nu = 0.2$ and $E = 10^8\,\mathrm{Pa}$ and the fluid parameters are the same as in the previous example, where $h_{\min} = 0.01\,\mathrm{m}$ and the time step is $\Delta t = 0.01$. Here, two injection stages are positioned at $(0\,\mathrm{m}, 0.25\,\mathrm{m})$ and $(0.25\,\mathrm{m}, 0\,\mathrm{m})$ on the hole boundary and we utilized Peaceman's well model [116] for the fluid injection. Fig. 17 illustrates the fluid filled fracture propagation handling multiple injection points with the pressure values for each time step.

5.3.3. *Fracture propagation in layers with different G_c values*

In addition, our approach can simulate the fracture propagation where the fracture is in a surrounded layered elastic media with different values of G_c. Here, we focus on fracture propagation from a soft layer to a rigid layer as studied in [117]. In the domain $\Lambda = (0, 4\,\mathrm{m})^2$, we separate the layers with different values for G_c. Here $G_c = 10\,\mathrm{Pa\,m}$ for $y > 3$, $y < 1$, $x > 3$ and $x < 1$ (the outer darker region in Fig. 18(a)), and $G_c = 1$ for $1 \leq y \leq 3$, and $1 \leq x \leq 3$.

The initial crack is centered at $(2\,\mathrm{m}, 2.05\,\mathrm{m})$ with the length $l = 0.225\,\mathrm{m}$. Here $h_{\min} = 0.011\,\mathrm{m}$ and the time steps are chosen as $\Delta t = 0.01$. The fluid is injected at the center of the crack and the fluid, well model, and the mechanical parameters are given as same as the previous wellbore example. We observe the kinking of the fracture when it approaches the rigid layer and subsequent fracture growing along the layer in Fig. 18.

5.3.4. *Fracture propagation and interaction with natural fractures*

Recently, we investigated the interactions between natural fractures and a two phase fluid filled fracture propagation [45] by using IPACS-version 5. A schematic setup for the numerical experiments is illustrated in

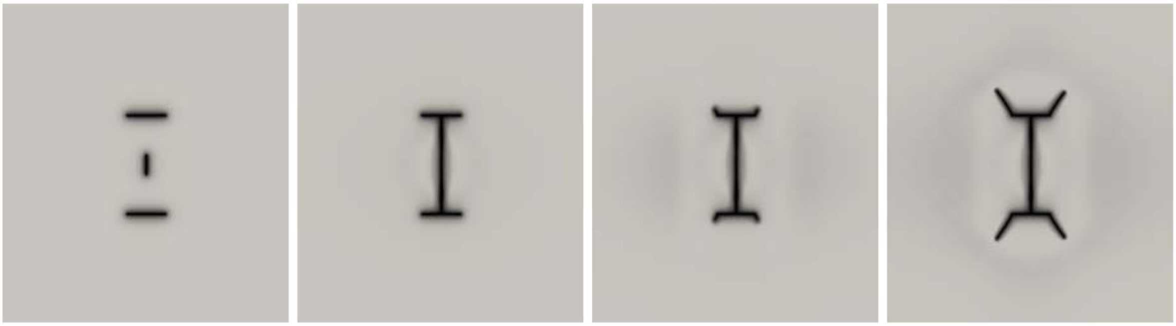

(a) $n = 1$ (b) $n = 30$ (c) $n = 70$ (d) $n = 100$

Fig. 19. Phase field values for propagating fractures for each time step n.

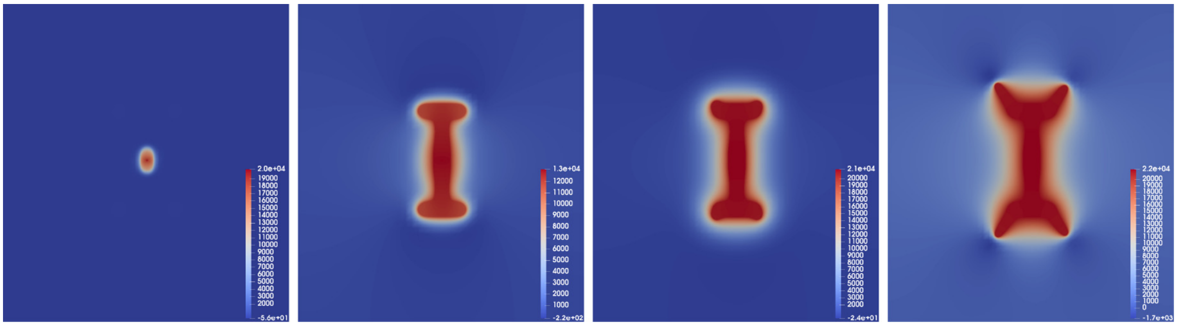

(a) $n = 2$ (b) $n = 30$ (c) $n = 70$ (d) $n = 100$

Fig. 20. Pressure values for propagating fractures for each time step n. We observe the pressure drop from (a) to (b), after the hydraulic fracture encounters the natural fractures. Then, additional pressure is required (c) to restart propagation from the tip of the natural fractures. (d) Moreover, the pressure decreases when the fracture starts to propagate then it increases again.

Fig. 19(a), where the natural fractures at the top and bottom, and the hydraulic fracture is placed at the middle. The location of the midpoint of the hydraulic fracture (injection point) is $(2\,\mathrm{m}, 2\,\mathrm{m})$ in the domain $\Lambda = (0, 2\,\mathrm{m})^2$. Then, two natural fractures are symmetrically placed with the length set as $0.5\,\mathrm{m}$, and the interaction angle is fixed as $\theta = 90°$.

The simulated phase-field values for the propagating fractures for each time step n are presented in Fig. 19. As the setup is symmetric, the propagation of the fracture is also symmetric. The fracture propagation speed from Fig. 19 (a) to (b) is much faster than Fig. 19(b) to (c) since it takes much longer time to initiate the branching of the fractures at the tip of the natural fractures in Fig. 19(c). The main reason for the difference in propagation speed is due to the pressure drop when the hydraulic fracture meets and joins with the natural fractures. This effect is also illustrated in Fig. 20, and the results show that additional pressure is required to initiate hydraulic fractures branching from the tip of natural fractures.

5.3.5. Comparing crack propagation using Newtonian versus power-law fluid models

Here, the Newtonian fracture flow is compared with the quasi-Newtonian model presented in a previous section. In the domain $\Lambda = (0, 4\,\mathrm{m})^2$, we set an initial fracture centered at $(2\,\mathrm{m}, 2\,\mathrm{m})$ with radius $r = 0.4\,\mathrm{m}$ with thickness of $2h_{\min}$. The mechanical parameters are $G_c = 1.0\mathrm{N/m}$, $\nu = 0.2$ and $E = 10^8\,\mathrm{Pa}$ in the homogeneous domain. The fluid is injected at the center of the fracture with the constant volume rate of $q_F = 200\,\mathrm{m}^3/\mathrm{s}$ for point source injection in the first 40 timesteps and then slightly reduced by $q_F = 200\,\mathrm{m}^3/\mathrm{s} \times (100 - n)/60$ (where n is the time step number) and $q_L = 0$. The fluid parameters are given as $\eta_F = \eta_R = 10^{-3}\,\mathrm{Ns/m}^2$, $\rho_R = \rho_F = 1000\,\mathrm{kg/m}^3$. The diagonal entry of the permeability $K_R = diag(k_R)$ is defined with its entry $k_R = 10^{-12}$, and all other parameters are $c_F = 10^{-10}$ and the Biot modulus is $M = 2.5 \times 10^8\,\mathrm{Pa}$. Here $h_{\min} = 0.022\,\mathrm{m}$ and the time step is $\Delta t = 0.01$, with $T = 3$ s.

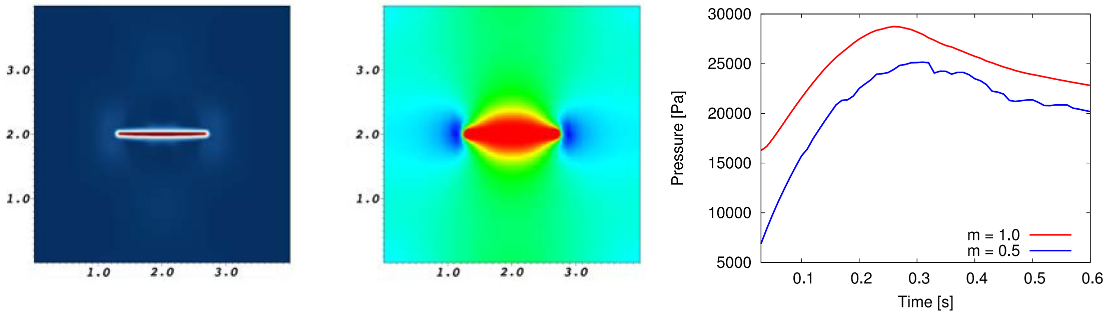

Fig. 21. Fracture at time $T = 0.5$ s with $m = 0.5$. Left: fracture path, middle pressure field, and at right we observe the pressure evolution for Newtonian and non-Newtonian flow.

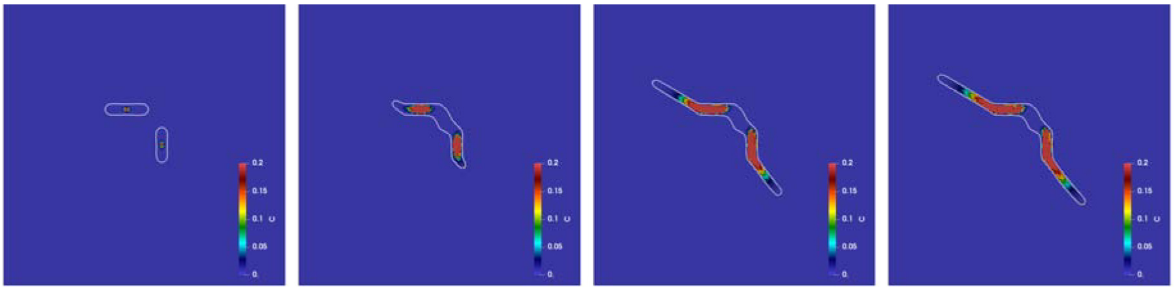

(a) $n = 1$ (b) $n = 40$ (c) $n = 80$ (d) $n = 100$

Fig. 22. Concentration values and joining of two fractures for each time step n. The solid contour line indicates the fracture, phase-field value $\varphi = 0.8$.

Two power law indexes $m = 1$ and $m = 0.5$ are tested in this example. We compared the length of the fracture and the highest pressure value for these two cases. We did not observe significant differences in the fracture length; see Fig. 21 and the pressure profile is comparable as well. However, a quantitative comparison shows that the entire pressure is lower using a non-Newtonian fluid flow model.

5.4. Test scenario 3: proppant transport and non-Newtonian flow inside the fracture

The fracture propagation is now coupled with the transport equation to simulate proppant in fluid filled fractures [33]. These numerical experiments are computed by IPACS-version 4, where the enriched Galerkin finite element scheme is employed.

5.4.1. Two fractures with proppant transport

In this example, we couple the transport equation and compute the concentration values in two initial fractures in arbitrary positions while they propagate due to injection. We emphasize the transport of concentration values within the joining and branching of the fractures.

Fig. 22 (left) presents the initial setup for the multiple fractures on the locally refined domain $\Lambda = (0, 4\,\mathrm{m})^2$. The right fracture is centered at $(2.25\,\mathrm{m}, 2\,\mathrm{m})$ with length $0.4\,\mathrm{m}$ and the left fracture is centered at $(1.75\,\mathrm{m}, 2.5\,\mathrm{m})$ with length $r = 0.5\,\mathrm{m}$. The mechanical parameters are $\nu = 0.2$ and $E = 10^8$ Pa for the homogeneous domain. Here the fluid is injected at the center of the fracture with the volume rate $q_F = 200\,\mathrm{m}^3/\mathrm{s}$. The discretization parameters are $\Delta t = 0.01$ and $h_{\min} = 0.054\,\mathrm{m}$.

Fig. 22 shows at each time step n of the concentration values with fractures propagating. Here the contour indicates the fracture ($\varphi = 0.8$) with the proppant moving with the fracture propagation ($Q = 100$).

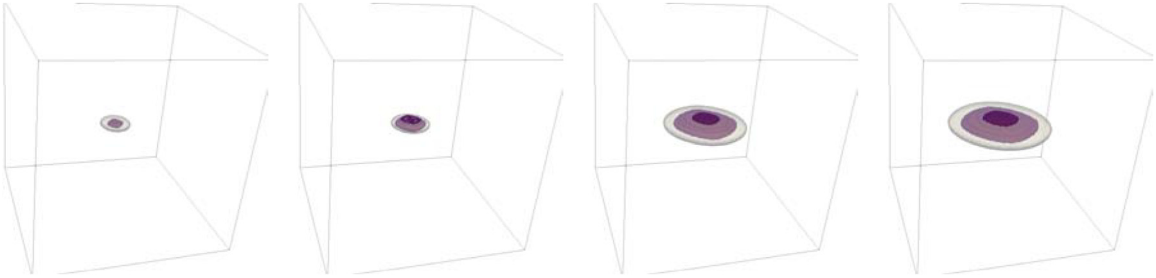

(a) $n = 1$ (b) $n = 10$ (c) $n = 50$ (d) $n = 80$

Fig. 23. Concentration values along with fracture propagation at each time step n.

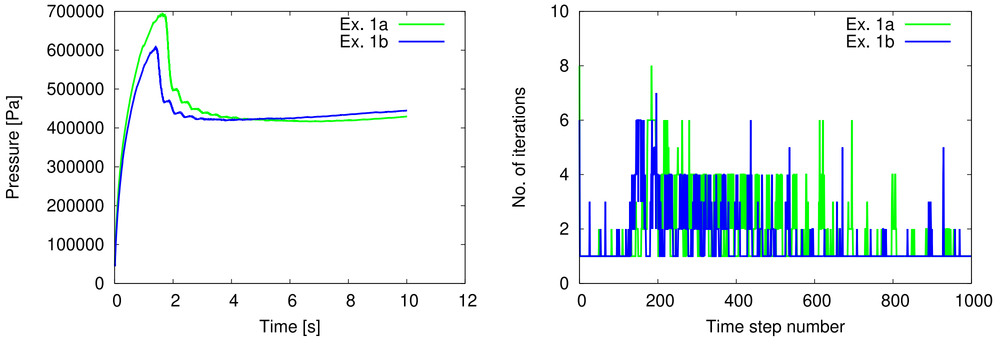

Fig. 24. Test scenario 4: Quantitative comparison of the evolutions of the maximum pressure and fixed-stress iterations. At the highest pressures, the values differ by about 15% while the difference is about 3% at the end at $T = 10$ s. From these data, we conclude a very good agreement and thus an independence of the model with respect to the geometry (i.e., here a rotation of the initial fracture).

5.4.2. *A three dimensional penny shape fracture with proppant*

In the three dimensional domain $\Lambda = (0, 4\,\text{m})^3$, the initial penny shape fracture is centered at $(2\,\text{m}, 2\,\text{m}, 2\,\text{m})$ on $y = 2\,\text{m}$ with the radius $r = 0.25\,\text{m}$. The fluid is injected at the center of the fracture and all the parameters are the same as in the previous two dimensional example. Here $h_{\min} = 0.054\,\text{m}$ and the time step is $\Delta t = 0.01$. Fig. 23 illustrates each step of the fracture propagation due to the injection of fluid with the transport of concentration where $Q = 250$. More realistic studies for the choice of Q and the flow model for the transport are ongoing.

5.5. *Test scenario 4: two-phase fracture flow*

We present numerical experiments by utilizing the two-phase fracture flow model developed in [34]. IPACS-version 5 is computed for the following examples. In Fig. 24, the final saturation distributions and the evolution of the maximum pressure are displayed. Two scenarios are studied: a fracture parallel to the x-axis and a diagonal fracture. Our results show that the fracture alignment does not alter the results, which was to be expected, but due to the mesh structure, it is not totally obvious. Moreover, in the right subfigure of Fig. 24, the number of fixed-stress iterations is shown. With a few number of iterations our algorithm converges. The pressure fields are plotted in Fig. 25.

5.6. *Test scenario 5: Coupling IPACS with IPARS (a reservoir simulator)*

A useful application of IPACS is to study the effects of hydraulic fractures in the production of oil and gas. We present some examples to demonstrate the explicit coupling of IPACS to IPARS (Integrated Parallel Accurate Reservoir Simulator) [15].

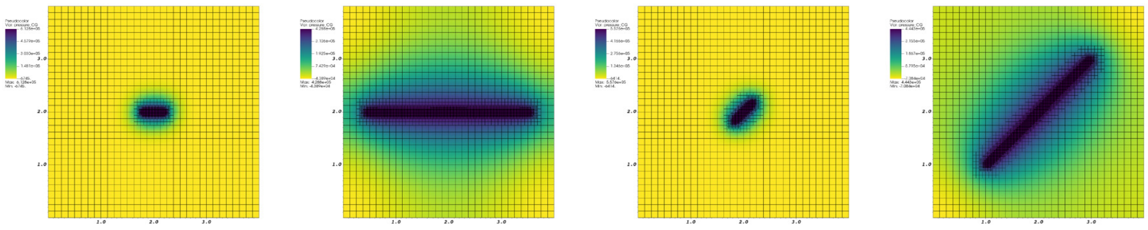

(a) (b) (c) (d)

Fig. 25. Pressure field of the two-phase flow example including the adaptively refined mesh. Going from left to right: straight fracture at steps 100 and 1000; diagonal fracture at the steps 100 and 1000.

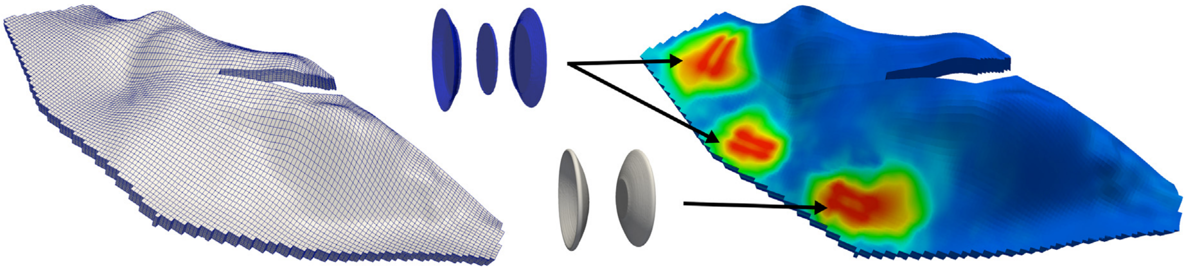

Fig. 26. Brugge field geometry with fractured injection wells. The fractures are computed with the IPACS fluid phase-field model and the reservoir data are obtained with IPARS. (For interpretation of the references to color in this figure legend, the reader is referred to the web version of this article.)

A synthetic case is generated from Brugge field geometry (see e.g. [118,119]) where the wells are augmented with hydraulic fractures propagated from IPACS. Here the use of fractured wells reduces the number of injection wells while improving sweep efficiency. The phase field fracture propagation model (IPACS), followed by production evaluation of reservoir, allows us to develop an intuitive understanding of recovery predictions and serves as a decision making tool for design, evaluation and long term field developments.

In Fig. 26 the Brugge field mesh and the simulated saturation values after 360 days by employing the fractures as the injection wells is shown. In the red colored regions, fractures obtained from the IPACS simulation are inserted.

5.7. Test scenario 6: Coupling with other simulators

In this section, we summarize the development of IPACS by coupling with other simulators. This emphasizes the capability of our algorithm as an efficient module which could be easily extracted and applied for different applications.

5.7.1. Using probability maps for natural fracture network

First, we illustrate some examples, where we coupled a natural fracture network obtained from field data with our phase-field fracture framework. Here, the initial condition for IPACS (in particular the phase-field function) for natural fracture network is obtained from a probability map [13,37]. The probability maps are based on surface deflections recorded using remote sensing sensors using InSAR (Interferometric Synthetic Aperture Radar) satellite and proxy methods [120]. This procedure is efficient in the sense that the probability map yields statistical values between 0 and 1 that can be interpolated as initial conditions for phase-field φ_0. IPACS results for fracture propagation are shown in Figs. 27 and 28. In case (a), one single hydraulic fracture is prescribed, while in case (b), two initial hydraulic fractures are shown. In Fig. 27 (left), the phase-field function and the pressure field in the very first time step are displayed. After 30 s the hydraulic fractures meet natural fractures and propagate. In Fig. 28, the two hydraulic fractures first join, and then grow.

(a) $T = 1s$ (b) $T = 30s$

Fig. 27. Case a. For each time (a) $T = 1$ s and (b) $T = 30$ s, we plot the phase field value (top) and the corresponding pressure value (bottom). For the phase field, blue indicates $\varphi = 0$ and red indicates $\varphi = 1$. We observe a single hydraulic fracture propagating and interacting with initial fractures. (For interpretation of the references to color in this figure legend, the reader is referred to the web version of this article.)

(a) $T = 1s$ (b) $T = 30s$

Fig. 28. Case b. In extension to Case 1, we prescribe two hydraulic fractures. As before, the fracture pattern (including branching and joining with natural fractures) and the corresponding pressure distribution are shown.

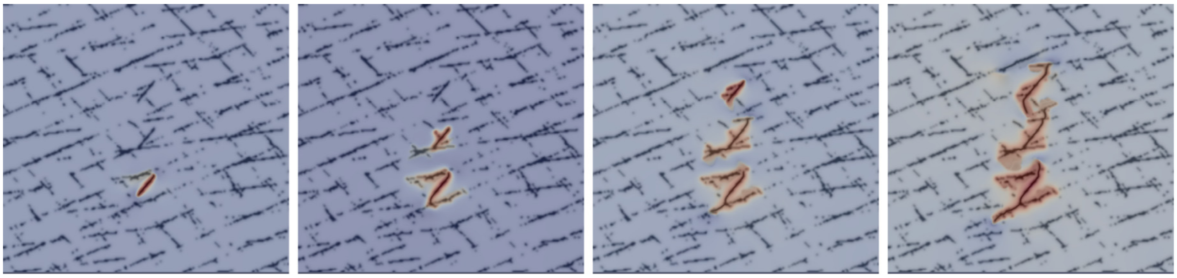

(a) $n = 10$ (b) $n = 40$ (c) $n = 60$ (d) $n = 80$

Fig. 29. On the top of the phase field values, layered pressure values are presented to emphasize different stages of the injections. First, the bottom well is activated at the beginning and the middle well is injected near $n = 40$. Finally, the injection for the top well started after $n = 60$.

In addition, IPACS can model different injection stages for hydraulic fractures. Fig. 29 illustrates an example of initial natural fracture network field provided by a probability map [37]. In this example, the injection stages are varied. This capability allows optimizing the delay between injection stages for maximizing the fractured area for oil and gas production.

We observe that the numerical tests in this subsection are challenging because of the interpolation of the initial phase-field condition and the very heterogeneous distribution of φ during the entire computation. Here, sufficiently fine meshes and regularization parameters must be used. In addition, such configurations pose challenges to the nonlinear and linear solvers, and the fracture width computation.

5.7.2. Coupling with the optimization tool UT-OPT

Next, we integrated IPACS with the optimization tool UT-OPT [44]. The aim was to obtain the optimal distance between fractures to maximize the fracture area and/or to perform history matching. Therein, the genetic algorithm

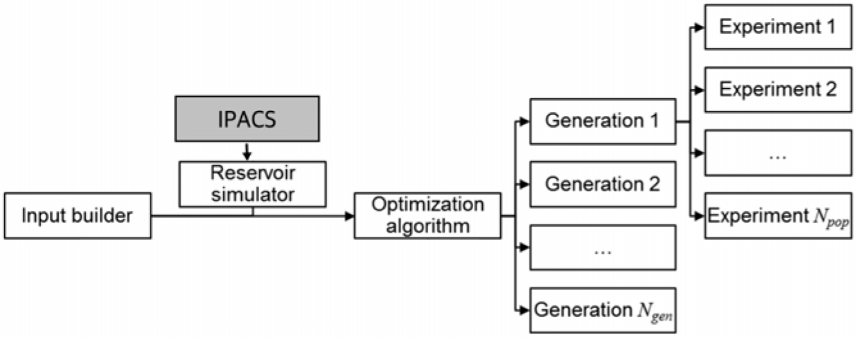

Fig. 30. A framework for the coupled IPACS and UT-OPT optimization tool.

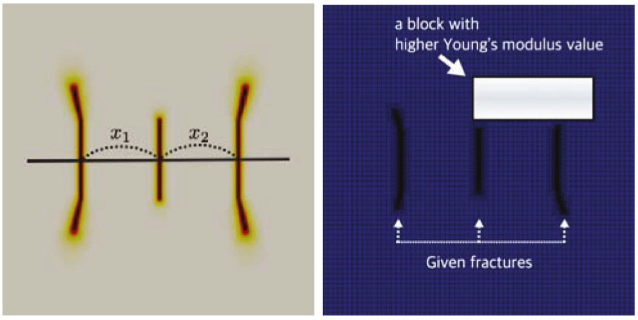

(a) (b)

Fig. 31. (a) An example of optimization problem; maximizing the fracture by choosing the optimal x_1 and x_2. (b) an example of minimization problem to find the position of the block with higher Young's modulus values when the fractures are given.

(GA) [121] was used as a global-objective optimizer and is referred to as UT-OPT (University of Texas Austin-Multiple Realization Optimizer [122]). Fig. 30 shows details of the algorithm. Performance of the coupled approach is provided with applications to numerical experiments related to maximizing production or reservoir history matching for emphasizing the capability of the framework.

Several numerical experiments are illustrated in [44] to show the capabilities of the coupled algorithm. The first two examples provide maximization problems, which is to find the optimal distance between the parallel fractures (as shown in Section 5.2.1) to maximize the fractured area (including the stress shadow effect), see Fig. 31(a). In addition, one minimization problem to find the heterogeneous Young's modulus values with given fractures is also presented (see Fig. 31(b)). All these examples ran 20 experiments concurrently in each generation, and every phase field fracture simulation is executed with 4 parallel processors.

6. Conclusions

In this work, we described the mathematical and numerical features of our software IPACS: an Integrated Phase-Field Advanced Crack Propagation Simulator. We derived the main features of coupling geomechanics with flow in porous media in which (possibly multiple) fractures are described using a phase-field technique.

The overall software is written in C++ and is based on the open-source finite element framework deal.II. The respective code versions of IPACS are outlined in Section 5.1 and a compact summary is given in Fig. 4. An important aspect is the numerically-sound overall coupling algorithm and physics-based discretization schemes. Parallel computing along with local mesh adaptivity allows for competitive wall time measurements. The IPACS software has been demonstrated with various representative test scenarios for two- and three-dimensional settings. The numerical robustness was shown in terms of a qualitative computational analysis adopting different mesh and time step sizes. Moreover, parts of the code are benchmarked against manufactured solutions such as configurations taken from Sneddon/Lowengrub [109]. These numerical examples show promising results for future extensions, which include more advanced physics such as multi-phase flow in fractures and the reservoir, respectively, treatment of flow-back and the prediction of hydraulic fracture geometries, frac-hits, and the application of surfactants for better production strategies.

Declaration of competing interest

The authors declare that they have no known competing financial interests or personal relationships that could have appeared to influence the work reported in this paper.

Acknowledgments

We thank Andro Mikelić (Université de Lyon), Baehyun Min (Ewha Womans University), Mohamad Jammoul (UT Austin), Timo Heister (Clemson University), Sanjay Srinivasan (Penn State) for their previous contributions and discussions.

The work of M.F. Wheeler is supported by the CSM, United States affiliates program and the NSF (National Science Foundation), United States grant *High-fidelty modeling of poromechanics with strong discontinuities* with the number 1911320. T. Wick is supported by the German Research Foundation, Priority Program 1748 (DFG SPP 1748) named *Reliable Simulation Techniques in Solid Mechanics. Development of Non-standard Discretization Methods, Mechanical and Mathematical Analysis* in the sub-project (WI 4367/2-1) under the number 392587580. Moreover, T. Wick thanks the Center for Subsurface Modeling for support during the stay in November 2019. The author S. Lee would like to thank the support from the Center for Subsurface Modeling, J. T. Oden Faculty Fellowship Research Program from the Oden Institute for Computational Engineering and Sciences at the University of Texas at Austin, United States, and the National Science Foundation, United States under Grant No. (NSF DMS-1913016).

References

[1] F.O. Alpak, A Multiphysics Fully-Coupled Flow and Geomechanics Simulation System with Hydraulic-Fracturing Simulation Capability, Vol. SPE-193825-MS, Society of Petroleum Engineers, 2019.
[2] J. Adachi, E. Siebrits, A. Peirce, J. Desroches, Computer simulation of hydraulic fractures, Int. J. Rock Mech. Min. Sci. 44 (5) (2007) 739–757.
[3] D. Mumford, J. Shah, Optimal approximations by piecewise smooth functions and associated variational problems, Commun. Pure Appl. Math. 42 (5) (1989) 577–685.
[4] L. Ambrosio, V. Tortorelli, Approximation of functionals depending on jumps by elliptic functionals via γ-convergence, Comm. Pure Appl. Math. 43 (1990) 999–1036.
[5] L. Ambrosio, V. Tortorelli, On the approximation of free discontinuity problems, Boll. Unione Mat. Ital. B 6 (1992) 105–123.
[6] T. Wick, S. Lee, M.F. Wheeler, 3D phase-field for pressurized fracture propagation in heterogeneous media, in: VI International Conference on Computational Methods for Coupled Problems in Science and Engineering 2015 Proceedings, 2015, May.
[7] T. Heister, M.F. Wheeler, T. Wick, A primal–dual active set method and predictor–corrector mesh adaptivity for computing fracture propagation using a phase-field approach, Comput. Methods Appl. Mech. Engrg. 290 (2015) 466–495.
[8] T. Wick, Goal functional evaluations for phase-field fracture using PU-based DWR mesh adaptivity, Comput. Mech. (2016) 1–19.
[9] S. Lee, M.F. Wheeler, T. Wick, Pressure and fluid-driven fracture propagation in porous media using an adaptive finite element phase field model, Comput. Methods Appl. Mech. Engrg. 305 (2016) 111–132.
[10] T. Heister, T. Wick, Parallel solution, adaptivity, computational convergence, and open-source code of 2d and 3d pressurized phase-field fracture problems, PAMM 18 (1) (2018) e201800353.
[11] A. Mikelić, M.F. Wheeler, T. Wick, A quasi-static phase-field approach to pressurized fractures, Nonlinearity 28 (5) (2015) 1371–1399.
[12] A. Mikelić, M.F. Wheeler, T. Wick, A phase-field method for propagating fluid-filled fractures coupled to a surrounding porous medium, SIAM Multiscale Model. Simul. 13 (1) (2015) 367–398.
[13] S. Lee, M.F. Wheeler, T. Wick, S. Srinivasan, Initialization of phase-field fracture propagation in porous media using probability maps of fracture networks, Mech. Res. Commun. 80 (2017) 16–23, Multi-Physics of Solids at Fracture.
[14] T. Wick, G. Singh, M. Wheeler, Pressurized fracture propagation using a phase-field approach coupled to a reservoir simulator, SPE Proc., 2013, SPE 168597-MS.
[15] T. Wick, G. Singh, M. Wheeler, Fluid-filled fracture propagation using a phase-field approach and coupling to a reservoir simulator, SPE J. 21 (03) (2016) 981–999.
[16] M.F. Wheeler, T. Wick, W. Wollner, An augmented-lagangrian method for the phase-field approach for pressurized fractures, Comput. Methods Appl. Mech. Eng. 271 (2014) 69–85.
[17] A. Mikelić, M.F. Wheeler, T. Wick, Phase-field modeling of a fluid-driven fracture in a poroelastic medium, Comput. Geosci. 19 (6) (2015) 1171–1195.

[18] B. Bourdin, C. Chukwudozie, K. Yoshioka, A variational approach to the numerical simulation of hydraulic fracturing, SPE Journal, in: Conference Paper 159154-MS, 2012.

[19] A. Chambolle, An approximation result for special functions with bounded variations, J. Math. Pures Appl. 83 (2004) 929–954.

[20] A. Mikelić, M. Wheeler, T. Wick, A Phase-Field Approach To the Fluid Filled Fracture Surrounded By a Poroelastic Medium, ICES Report 13–15, 2013, Jun.

[21] A. Mikelić, M. Wheeler, T. Wick, Phase-Field Modeling of Pressurized Fractures in a Poroelastic Medium, ICES Report 14–18, 2014, Jun.

[22] A. Mikelić, M.F. Wheeler, T. Wick, Phase-field modeling through iterative splitting of hydraulic fractures in a poroelastic medium, GEM - Int. J. Geomath. 10 (1) (2019).

[23] S. Almi, G.D. Maso, R. Toader, Quasi-static crack growth in hydraulic fracture, Nonlinear Anal. TMA 109 (2014) 301–318.

[24] T. Wick, An error-oriented Newton/inexact augmented Lagrangian approach for fully monolithic phase-field fracture propagation, SIAM J. Sci. Comput. 39 (4) (2017) B589–B617.

[25] T. Wick, Modified Newton methods for solving fully monolithic phase-field quasi-static brittle fracture propagation, Comput. Methods Appl. Mech. Engrg. 325 (2017) 577–611.

[26] C. Engwer, L. Schumacher, A phase field approach to pressurized fractures using discontinuous Galerkin methods, Math. Comput. Simulation 137 (2017) 266–285.

[27] C. Miehe, S. Mauthe, Phase field modeling of fracture in multi-physics problems. part iii. crack driving forces in hydro-poro-elasticity and hydraulic fracturing of fluid-saturated porous media, Comput. Methods Appl. Mech. Engrg. 304 (2016) 619–655.

[28] C. Miehe, S. Mauthe, S. Teichtmeister, Minimization principles for the coupled problem of Darcy Biot-type fluid transport in porous media linked to phase field modeling of fracture, J. Mech. Phys. Solids 82 (2015) 186–217.

[29] B. Markert, Y. Heider, Coupled multi-field continuum methods for porous media fracture, in: Recent Trends in Computational Engineering-CE2014, Springer, 2015, pp. 167–180.

[30] Y. Heider, B. Markert, A phase-field modeling approach of hydraulic fracture in saturated porous media, Mech. Res. Commun. 80 (2017) 38–46, Multi-Physics of Solids at Fracture.

[31] Z.A. Wilson, C.M. Landis, Phase-field modeling of hydraulic fracture, J. Mech. Phys. Solids 96 (2016) 264–290.

[32] C. Chukwudozie, B. Bourdin, K. Yoshioka, A variational phase-field model for hydraulic fracturing in porous media, Comput. Methods Appl. Mech. Engrg. 347 (2019) 957–982.

[33] S. Lee, A. Mikelić, M.F. Wheeler, T. Wick, Phase-field modeling of proppant-filled fractures in a poroelastic medium, Comput. Methods Appl. Mech. Engrg. 312 (2016) 509–541.

[34] S. Lee, A. Mikelić, M. Wheeler, T. Wick, Phase-field modeling of two phase fluid filled fractures in a poroelastic medium, Multiscale Model. Simul. 16 (4) (2018) 1542–1580.

[35] C.J. van Duijn, A. Mikelić, T. Wick, A monolithic phase-field model of a fluid-driven fracture in a nonlinear poroelastic medium, Math. Mech. Solids 24 (5) (2019) 1530–1555.

[36] T. Cajuhi, L. Sanavia, L. De Lorenzis, Phase-field modeling of fracture in variably saturated porous media, Comput. Mech. (2017).

[37] M.F. Wheeler, S. Srinivasan, S. Lee, M. Singh, et al., Unconventional reservoir management modeling coupling diffusive zone/phase field fracture modeling and fracture probability maps, in: SPE Reservoir Simulation Conference, Society of Petroleum Engineers, 2019.

[38] T. Wick, Coupling fluid–structure interaction with phase-field fracture, J. Comput. Phys. 327 (2016) 67–96.

[39] S. Lee, M.F. Wheeler, T. Wick, Iterative coupling of flow, geomechanics and adaptive phase-field fracture including level-set crack width approaches, J. Comput. Appl. Math. 314 (2017) 40–60.

[40] D. Santillan, R. Juanes, L. Cueto-Felgueroso, Phase field model of fluid-driven fracture in elastic media: Immersed-fracture formulation and validation with analytical solutions, J. Geophys. Res.: Solid Earth 122 (2017) 2565–2589.

[41] T. Almani, S. Lee, M.F. Wheeler, T. Wick, Multirate Coupling for Flow and Geomechanics Applied To Hydraulic Fracturing using an Adaptive Phase-Field Technique. Vol. SPE-182610-MS, Society of Petroleum Engineers, 2017.

[42] N. Noii, T. Wick, A phase-field description for pressurized and non-isothermal propagating fractures, Comput. Methods Appl. Mech. Engrg. 351 (2019) 860–890.

[43] S. Shiozawa, S. Lee, M.F. Wheeler, The effect of stress boundary conditions on fluid-driven fracture propagation in porous media using a phase-field modeling approach, Int. J. Numer. Anal. Methods Geomech. 43 (6) (2019) 1316–1340.

[44] S. Lee, B. Min, M.F. Wheeler, Optimal design of hydraulic fracturing in porous media using the phase field fracture model coupled with genetic algorithm, Comput. Geosci. 22 (3) (2018) 833–849.

[45] S. Lee, M.F. Wheeler, Modeling interactions of natural and two phase fluid filled fracture propagation in porous media, Comput. Geosci. (2020) http://dx.doi.org/10.1007/s10596-020-09975-0.

[46] Y. Heider, S. Reiche, P. Siebert, B. Markert, Modeling of hydraulic fracturing using a porous-media phase-field approach with reference to experimental data, Eng. Fract. Mech. 202 (2018) 116–134.

[47] S. Zhou, X. Zhuang, T. Rabczuk, Phase-field modeling of fluid-driven dynamic cracking in porous media, Comput. Methods Appl. Mech. Engrg. 350 (2019) 169–198.

[48] A. Griffith, The phenomena of rupture and flow in solids, Phil. Trans. R. Soc. A 221 (1921) 163–198.

[49] G. Francfort, J.-J. Marigo, Revisiting brittle fracture as an energy minimization problem, J. Mech. Phys. Solids 46 (8) (1998) 1319–1342.

[50] H. Amor, J.-J. Marigo, C. Maurini, Regularized formulation of the variational brittle fracture with unilateral contact: Numerical experiments, J. Mech. Phys. Solids 57 (2009) 1209–1229.

[51] C. Miehe, F. Welschinger, M. Hofacker, Thermodynamically consistent phase-field models of fracture: variational principles and multi-field fe implementations, Int. J. Numer. Methods Eng. 83 (2010) 1273–1311.

[52] C. Miehe, M. Hofacker, F. Welschinger, A phase field model for rate-independent crack propagation: Robust algorithmic implementation based on operator splits, Comput. Methods Appl. Mech. Engrg. 199 (2010) 2765–2778.

[53] B. Bourdin, G. Francfort, J.-J. Marigo, Numerical experiments in revisited brittle fracture, J. Mech. Phys. Solids 48 (4) (2000) 797–826.

[54] A. Braides, Approximation of Free-Discontinuity Problems, in: Lecture Notes in Mathematics No. 1694, Springer Verlag, Berlin, 1998.

[55] M. Ambati, T. Gerasimov, L. De Lorenzis, Phase-field modeling of ductile fracture, Comput. Mech. (2015) 1–24.

[56] F. Meng, T. Wick, J. Yan, A phase-field description for mixed-mode fracture propagation, Hannover : Institutionelles Repositorium der Leibniz Universität Hannover (2019) http://dx.doi.org/10.15488/5369, 40 S.

[57] M. Biot, General theory of three-dimensional consolidation, J. Appl. Phys. 12 (2) (1941) 155–164.

[58] I. Tolstoy, Acoustics, elasticity, and thermodynamics of porous media, in: Twenty-One Papers By M.a. Biot, Acoustical Society of America, New York, 1992.

[59] J.L. Lions, E. Magenes, Non-Homogeneous Boundary Value Problems and Applications, in: Grundlehren der mathematischen Wissenschaften, vol. 181, Springer, 1972.

[60] O. Ladyzhenskaja, V. Solonnikov, N. Uralceva, Linear and Quasi-Linear Equations of Parabolic Type, in: Translations of mathematical monographs, vol. 23, AMS, 1968.

[61] B. Ganis, V. Girault, M. Mear, G. Singh, M. Wheeler, Modeling Fractures in a Poro-Elastic Medium, Technical Report ICES REPORT 13–09, The University of Texas at Austin, 2013.

[62] B. Lecampion, E. Detournay, An implicit algorithm for the propagation of hydraulic fracture with a fluid lag, Comput. Methods Appl. Mech. Engrg. 196 (2007) 4863–4880.

[63] B.A. Schrefler, S. Secchi, L. Simoni, On adaptive refinement techniques in multi-field problems including cohesive fracture, Comput. Methods Appl. Mech. Engrg. 195 (2006) 444–461.

[64] A.Z. Szeri, Fluid Film Lubrication, Cambridge University Press, 2010.

[65] D. Drew, S. Passman, Theory of Multicomponent Fluids. Applied Mathematical Sciences, Springer, 1999.

[66] P.E. Clark, F.S. Manning, J.A. Quadir, N. Guler, Prop transport in vertical fractures, 1981, SPE-10261-MS.

[67] A.A. Daneshy, Numerical solution of sand transport in hydraulic fracturing, 1978, SPE-5636-MS.

[68] R.J. Clifton, J.-J. Wang, Multiple fluids, proppant transport, and thermal effects in three-dimensional simulation of hydraulic fracturing, 1988, SPE-18198-MS.

[69] E. Novotny, Proppant transport, 1977, SPE-6813-MS.

[70] G. Govier, K. Aziz, The Flow of Complex Mixtures in Pipes, Van Nostrand Reinhold Co., 1972.

[71] R.D. Barree, M.W. Conway, Experimental and numerical modeling of convective proppant transport, 1994, SPE-28564-MS.

[72] P.E. Clark, J.A. Quadir, Prop transport in hydraulic fractures: A critical review of particle settling velocity equations, 1981, SPE-9866-MS.

[73] L.A. Vadimovich, Models for proppant transport and deposition in hydraulic fracture simulation: A review of the state of the art, in: SINTEF rapport; 2011.057, 2011.

[74] E. Dontsov, A. Peirce, Proppant transport in hydraulic fracturing: Crack tip screen-out in kgd and p3d models, Int. J. Solids Struct. 63 (2015) 206–218.

[75] T. Arbogast, M. Juntunen, J. Pool, M.F. Wheeler, A discontinuous Galerkin method for two-phase flow in a porous medium enforcing H (div) velocity and continuous capillary pressure, Comput. Geosci. 17 (6) (2013) 1055–1078.

[76] Z. Chen, G. Huan, Y. Ma, Computational Methods for Multiphase Flows in Porous Media, SIAM, 2006.

[77] H. Hoteit, A. Firoozabadi, Numerical modeling of two-phase flow in heterogeneous permeable media with different capillarity pressures, Adv. Water Resour. 31 (1) (2008) 56–73.

[78] M.F. El-Amin, J. Kou, S. Sun, A. Salama, An iterative implicit scheme for nanoparticles transport with two-phase flow in porous media, Procedia Comput. Sci. 80 (2016) 1344–1353.

[79] S. Lee, M.F. Wheeler, Enriched Galerkin approximations for two phase flow in porous media with capillary pressure, J. Comput. Phys. 367 (2018) 65–86.

[80] T. Nguyen, J. Yvonnet, Q.-Z. Zhu, M. Bornert, C. Chateau, A phase-field method for computational modeling of interfacial damage interacting with crack propagation in realistic microstructures obtained by microtomography, Comput. Methods Appl. Mech. Engrg. 312 (2016) 567–595, Phase Field Approaches to Fracture.

[81] S. Sun, J. Liu, A locally conservative finite element method based on piecewise constant enrichment of the continuous galerkin method, SIAM J. Sci. Comput. 31 (4) (2009) 2528–2548.

[82] S. Lee, Y.-J. Lee, M.F. Wheeler, A locally conservative enriched Galerkin approximation and efficient solver for elliptic and parabolic problems, SIAM J. Sci. Comput. 38 (3) (2016) A1404–A1429.

[83] J. Choo, S. Lee, Enriched galerkin finite elements for coupled poromechanics with local mass conservation, Comput. Methods Appl. Mech. Engrg. 341 (2018) 311–332.

[84] S. Lee, M.F. Wheeler, Adaptive enriched Galerkin methods for miscible displacement problems with entropy residual stabilization, J. Comput. Phys. 331 (2017) 19–37.

[85] P. Mital, T. Wick, M.F. Wheeler, G. Pencheva, Discontinuous and enriched galerkin methods for phase-field fracture propagation in elasticity, in: B. Karasözen, M. Manguoğlu, M. Tezer-Sezgin, S. Göktepe, Ö. Uğur (Eds.), Numerical Mathematics and Advanced Applications ENUMATH, Springer International Publishing, Cham, 2015.

[86] B. Riviere, Discontinuous Galerkin Methods for Solving Elliptic and Parabolic Equations: Theory and Implementation, SIAM, 2008.

[87] L. Cappanera, B. Rivière, Discontinuous galerkin method for solving the black-oil problem in porous media, Numer. Methods Partial Differential Equations 35 (2) (2019) 761–789.

[88] N. Castelletto, J.A. White, H.A. Tchelepi, Accuracy and convergence properties of the fixed-stress iterative solution of two-way coupled poromechanics, Int. J. Numer. Anal. Methods Geomech. 39 (14) (2015) 1593–1618.

[89] J. Kim, H. Tchelepi, R. Juanes, Stability, accuracy, and efficiency of sequentiel methods for flow and geomechanics, SPE J. 16 (2) (2011) 249–262.

[90] J. Kim, H. Tchelepi, R. Juanes, Stability and convergence of sequentiel methods for coupled flow and geomechanics: fixed-stress and fixed-strain splits, Comput. Methods Appl. Mech. Eng. 200 (13–16) (2011) 1591–1606.

[91] A. Mikelić, B. Wang, M.F. Wheeler, Numerical convergence study of iterative coupling for coupled flow and geomechanics, Comput. Geosci. 18 (3–4) (2014) 325–341.

[92] A. Mikelić, M.F. Wheeler, Convergence of iterative coupling for coupled flow and geomechanics, Comput. Geosci. 17 (3) (2012) 455–462.

[93] A. Settari, F. Mourits, A coupled reservoir and geomechanical simulation system, SPE J. 3 (3) (1998) 219–226.

[94] A. Settari, D.A. Walters, Advances in coupled geomechanical and reservoir modeling with applications to reservoir compaction, SPE J. 6 (3) (2001) 334–342.

[95] Vivette Girault, Mary F. Wheeler, Tameem Almani, Saumik Dana, A priori error estimates for a discretized poro-elastic-elastic system solved by a fixed-stress algorithm, Oil Gas Sci. Technol. - Rev. IFP Energies nouvelles 74 (2019) 24.

[96] X. Lu, M.F. Wheeler, Three-way coupling of multiphase flow and poromechanics in porous media, J. Comput. Phys. (2019) 109053.

[97] R. Dean, X. Gai, C. Stone, S. Minkoff, A comparison of techniques for coupling porous flow and geomechanics, 2006, pp. 132–140, SPE-79709-MS.

[98] R. Dean, J. Schmidt, Hydraulic-fracture predictions with a fully coupled reservoir simulator, SPE J. 14 (4) (2009) 707–714.

[99] L.Y. Chin, L.K. Thomas, J.E. Sylte, R.G. Pierson, Iterative coupled analysis of geomechanics and fluid flow for rock compaction in reservoir simulation, Oil Gas Sci. Technol. 57 (5) (2002) 485–497.

[100] M. Mainguy, P. Longuemare, Coupling fluid flow and rock mechanics: formulations of the partial coupling between reservoir and geomechanics simulators, Oil Gas Sci. Technol.- Rev. IFP 57 (4) (2002) 355–367.

[101] J. Kim, H.A. Tchelepi, R. Juanes, Stability, accuracy, and efficiency of sequential methods for coupled flow and geomechanics, in: The SPE Reservoir Simulation Symposium, Houston, Texas, 2009, SPE119084.

[102] V. Girault, K. Kumar, M.F. Wheeler, Convergence of iterative coupling of geomechanics with flow in a fractured poroelastic medium, Comput. Geosci. (2016) 1–15.

[103] J. Both, M. Borregales, J. Nordbotten, K. Kumar, F. Radu, Robust fixed stress splitting for biot's equations in heterogeneous media, Appl. Math. Lett. 68 (2017) 101–108.

[104] T.M. Almani, Efficient Algorithms for Flow Models Coupled with Geomechanics for Porous Media Applications (Ph.D. thesis), The University of Texas at Austin, 2016.

[105] T. Almani, K. Kumar, G. Singh, M. Wheeler, Stability of multirate explicit coupling of geomechanics with flow in a poroelastic medium, Comput. Math. Appl. 78 (8) (2019) 2682–2699.

[106] I. Rybak, J. Magiera, R. Helmig, C. Rohde, Multirate time integration for coupled saturated/unsaturated porous medium and free flow systems, Comput. Geosci. 19 (2) (2015) 299–309.

[107] M. Hintermüller, K. Ito, K. Kunisch, The primal–dual active set strategy as a semismooth Newton method, SIAM J. Optim. 13 (3) (2002) 865–888.

[108] M. Heroux, R. Bartlett, V.H.R. Hoekstra, J. Hu, T. Kolda, R. Lehoucq, K. Long, R. Pawlowski, E. Phipps, A. Salinger, H. Thornquist, R. Tuminaro, J. Willenbring, A. Williams, An Overview of Trilinos, Technical Report SAND2003-2927, Sandia National Laboratories, 2003.

[109] I.N. Sneddon, M. Lowengrub, Crack Problems in the Classical Theory of Elasticity, in: SIAM series in Applied Mathematics, John Wiley and Sons, Philadelphia, 1969.

[110] K. Mang, T. Wick, Numerical Methods for Variational Phase-Field Fracture Problems, Institutionelles Repositorium der Leibniz Universität Hannover, Hannover, 2019, http://dx.doi.org/10.15488/5129.

[111] W. Bangerth, D. Davydov, T. Heister, L. Heltai, G. Kanschat, M. Kronbichler, M. Maier, B. Turcksin, D. Wells, The `deal.II` library, version 8.4, J. Numer. Math. 24 (2016).

[112] W. Bangerth, R. Hartmann, G. Kanschat, deal.II – a general purpose object oriented finite element library, ACM Trans. Math. Software 33 (4) (2007) 24/1–24/27.

[113] D. Arndt, W. Bangerth, T.C. Clevenger, D. Davydov, M. Fehling, D. Garcia-Sanchez, G. Harper, T. Heister, L. Heltai, M. Kronbichler, R.M. Kynch, M. Maier, J.-P. Pelteret, B. Turcksin, D. Wells, The `deal.II` library, version 9.1, J. Numer. Math. 27 (4) (2019) 203–213.

[114] C. Burstedde, L.C. Wilcox, O. Ghattas, P4est: Scalable algorithms for parallel adaptive mesh refinement on forests of octrees, SIAM J. Sci. Comput. 33 (3) (2011) 1103–1133.

[115] S. Castonguay, M. Mear, R. Dean, J. Schmidt, Predictions of the growth of multiple interacting hydraulic fractures in three dimensions, 2013, pp. 1–12, SPE-166259-MS.

[116] Z. Chen, Y. Zhang, Well flow models for various numerical methods, Int. J. Numer. Anal. Model. 6 (3) (2009) 375–388.

[117] H. Wu, A. Chudnovsky, G.K. abd, J.D. Wong, A map of fracture behavior in the vicinity of an interface, 2004.

[118] E. Peters, R. Arts, G. Brouwer, C. Geel, Results of the Brugge benchmark study for flooding optimisation and history matching, in: SPE Reservoir Simulation Symposium, 2009, SPE 119094-MS.

[119] C. Chen, Y. Wang, G. Li, Closed-loop reservoir management on the brugge test case, Comput. Geosci. 14 (2010) 691–703.

[120] A. Nwachukwu, Model Selection for CO_2 Sequestration using Surface Deflection and Injection Data (Master's thesis), The University of Texas at Austin, 2015.

[121] D.E. Goldberg, Genetic Algorithms in Search, Optimization, and Machine Learning, Addison-Wesley Professional, Reading, 1989.

[122] B. Min, M.F. Wheeler, A.Y. Sun, Parallel multiobjective optimization for the coupled compositional/geomechanical modeling of pulse testing, in: SPE Reservoir Simulation Conference, Society of Petroleum Engineers, 2017.